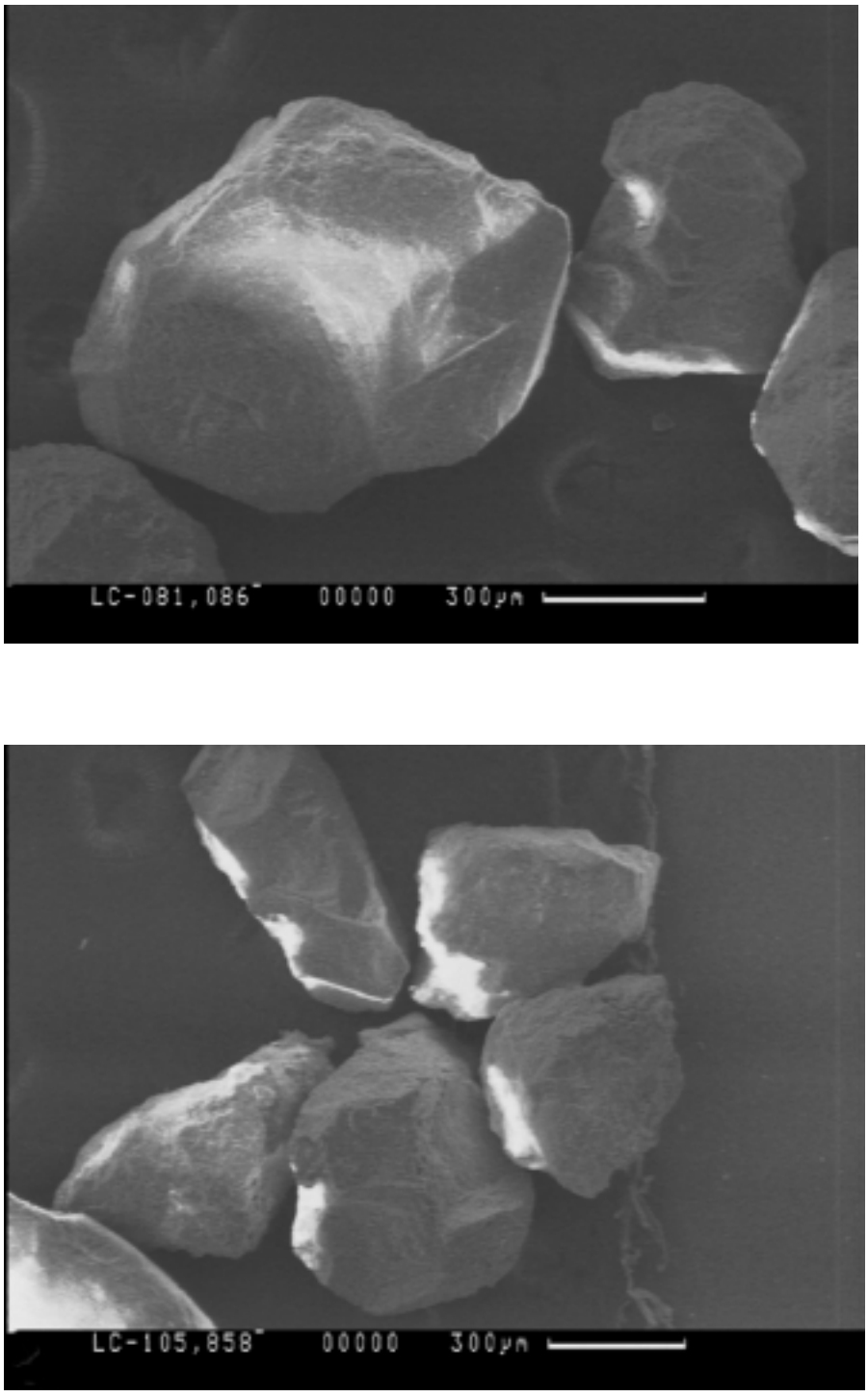

Figure 3.1 Scanning Electron Photographs of Light Castle Sand

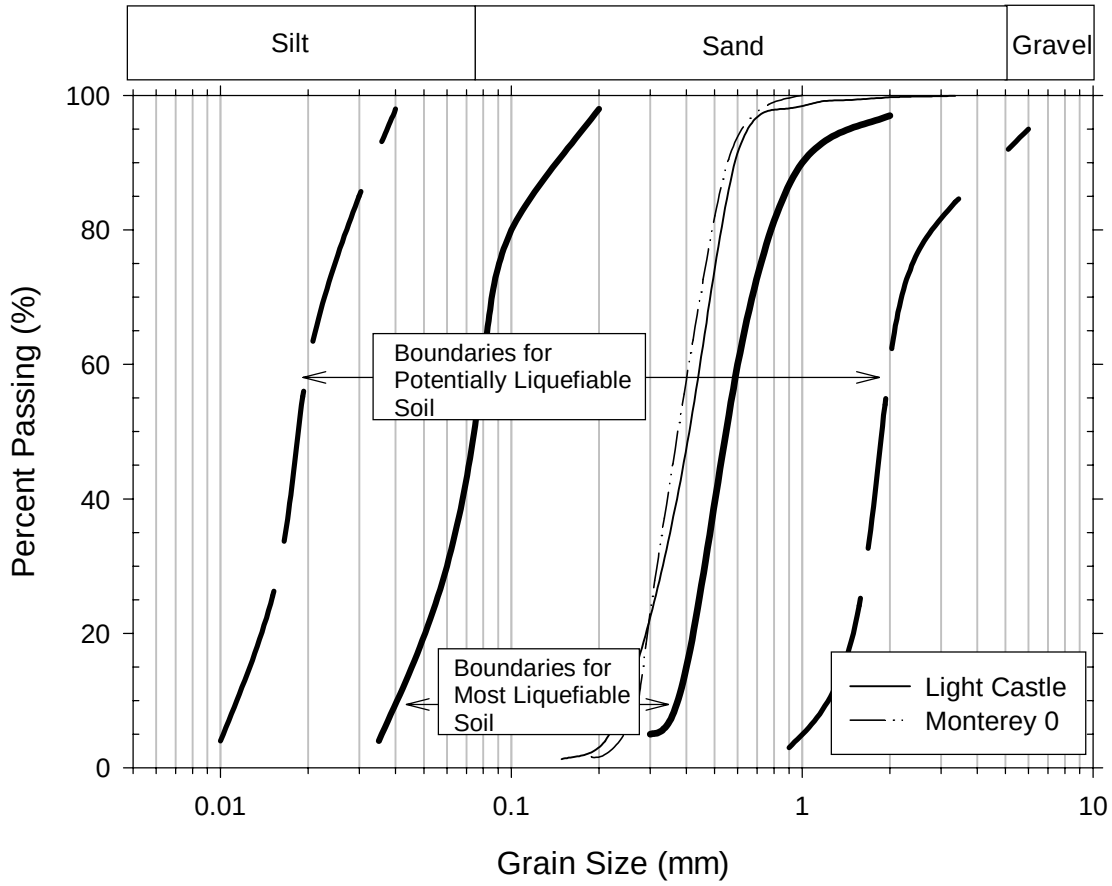

Figure 3.2 Grain Size Distribution Curves for Light Castle and Monterey 0 Sands (Modified from Ishihara 1993)

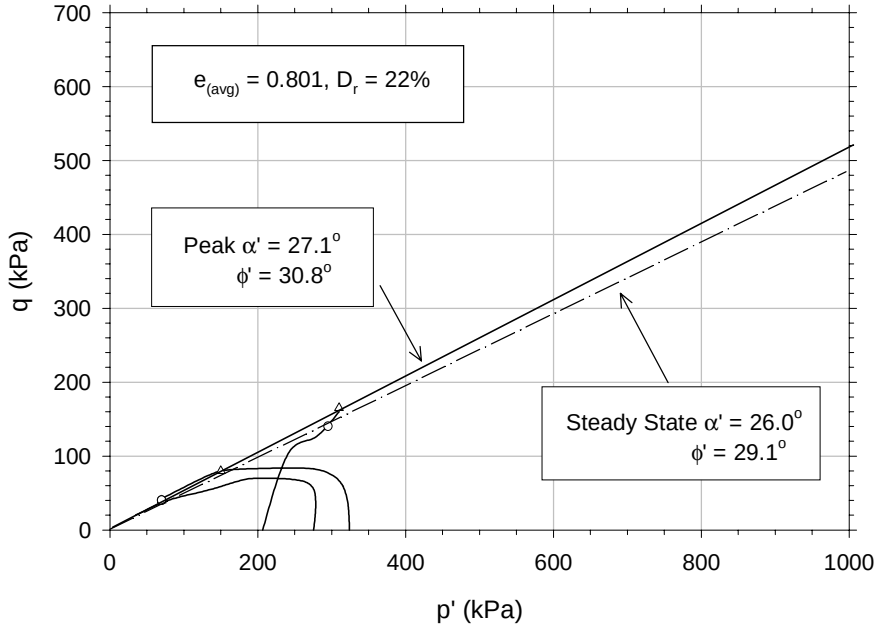

a) Loose (Adapted from Porter (1998))

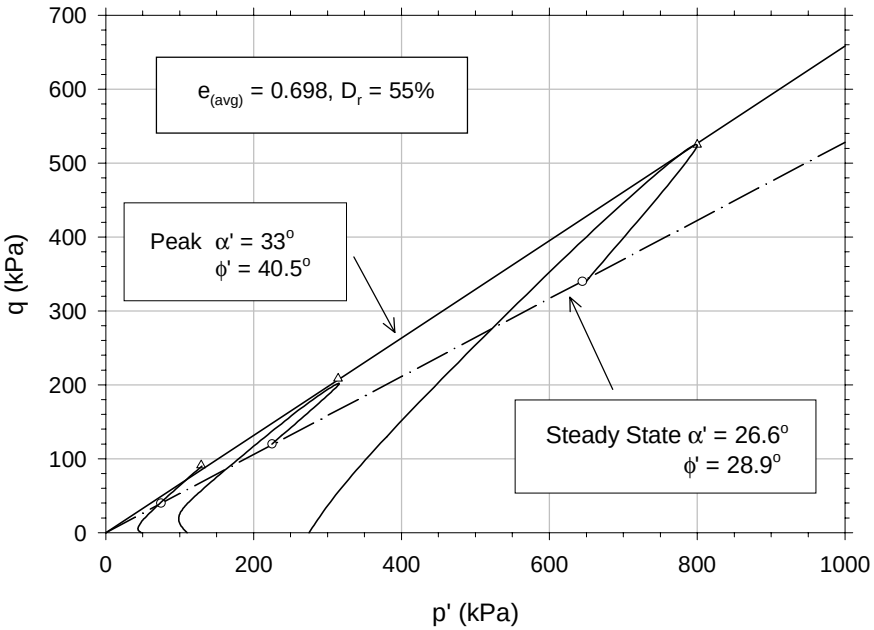

b) Medium Dense

Figure 3.3 Effective Stress Paths for ICU Triaxial Tests in Light Castle Sand

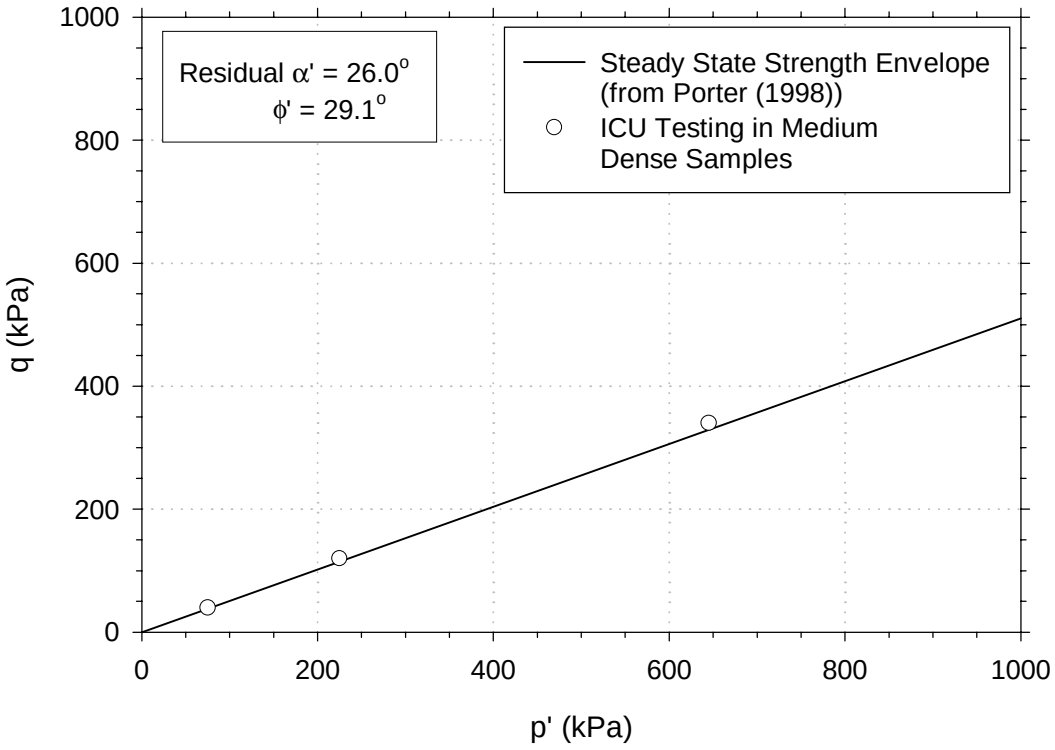

Figure 3.4 Steady State Failure Envelope for Light Castle Sand Based on ICU Triaxial Tests

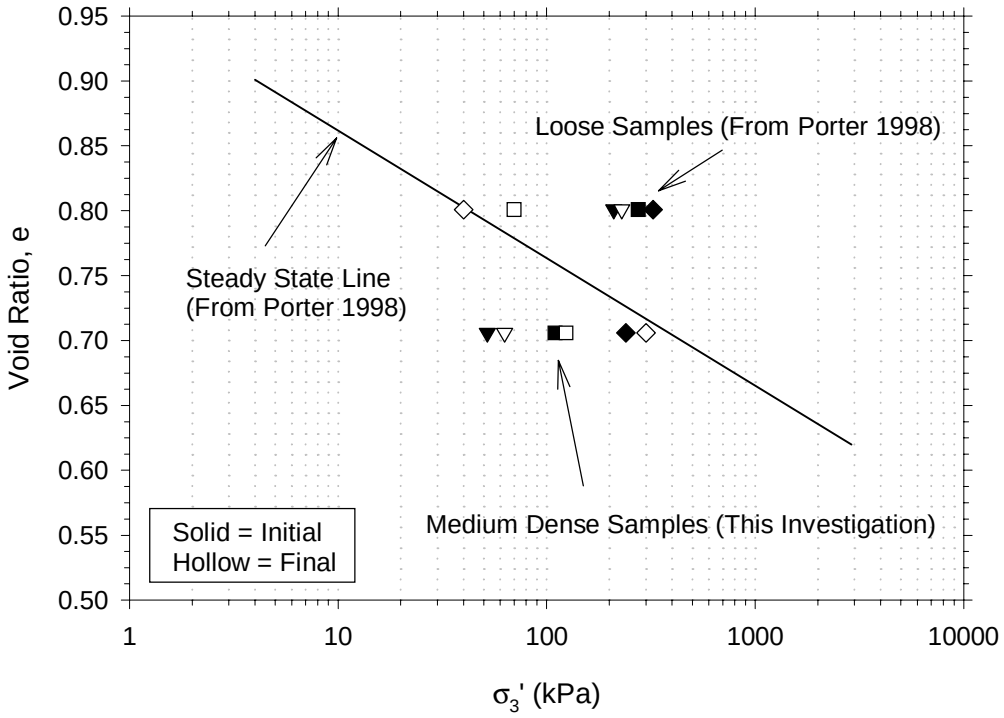

Figure 3.5 Steady State Line Generated for Light Castle Sand Based on ICU Triaxial Tests

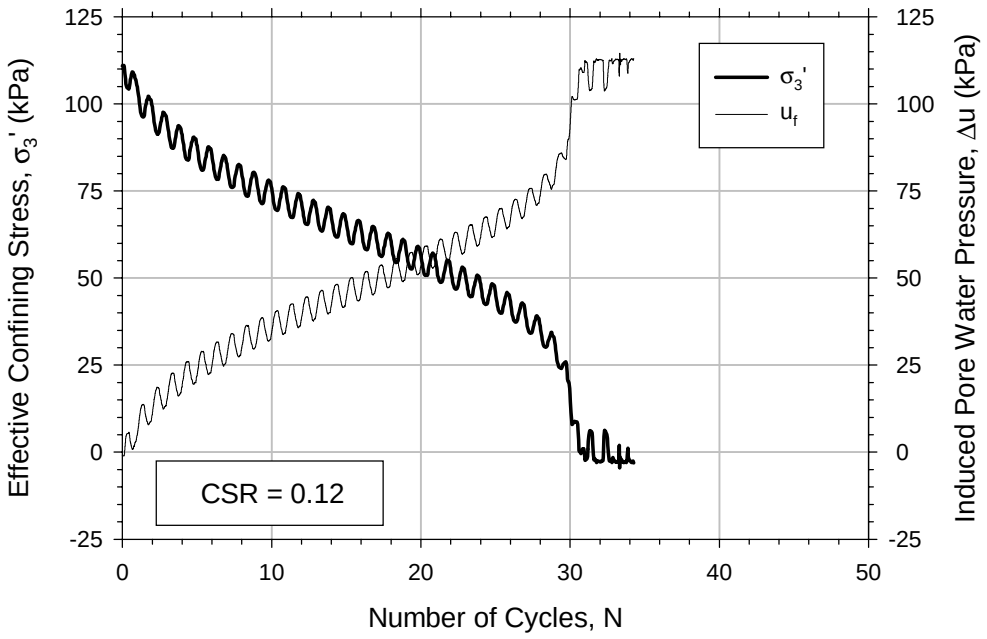

a) Effective Stress

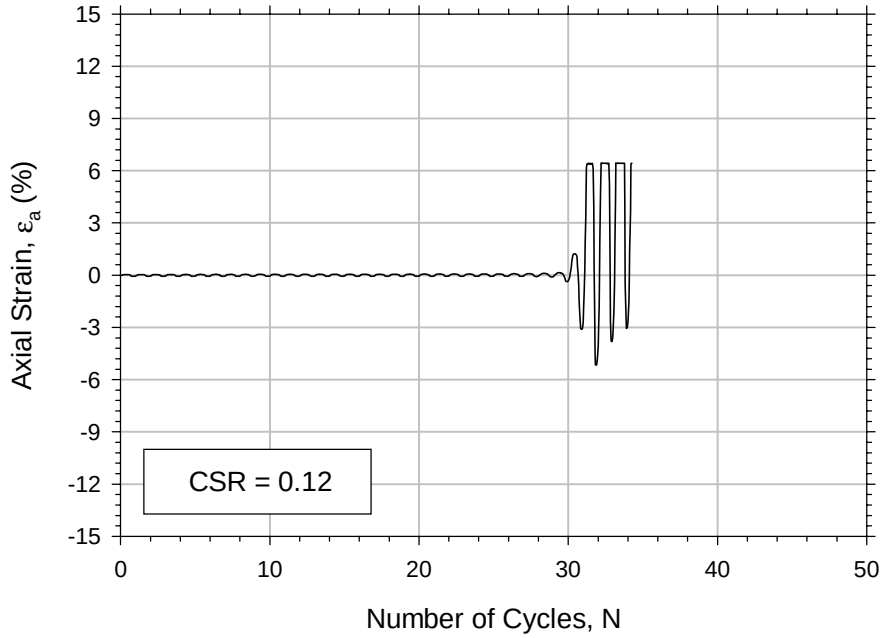

b) Axial Strain

Figure 3.6 Cyclic Triaxial Test Results for Loose Samples at CSR = 0.12

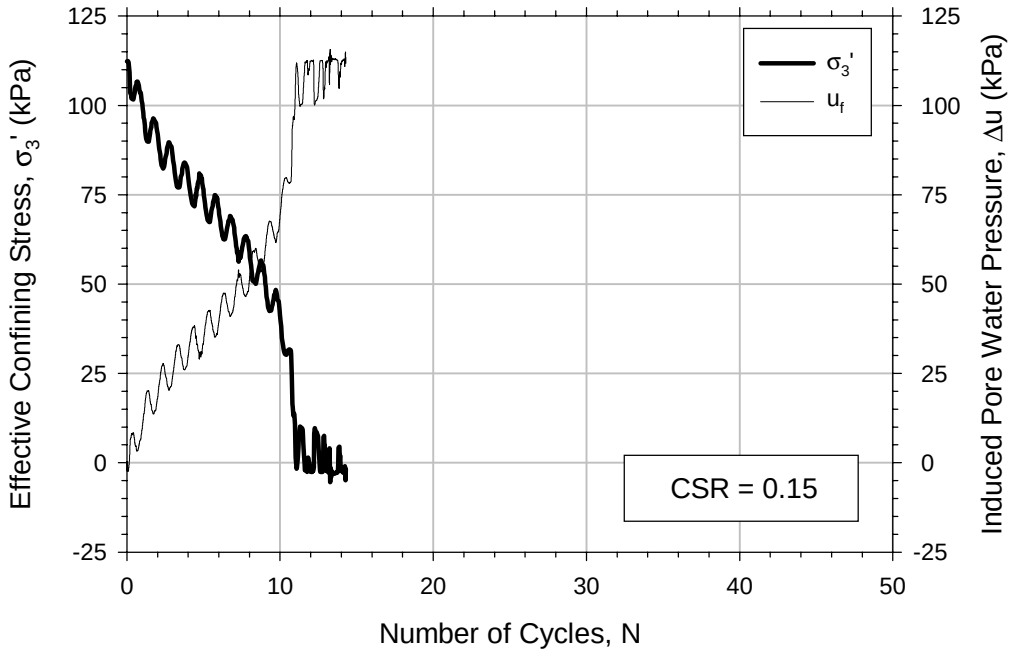

a) Effective Stress

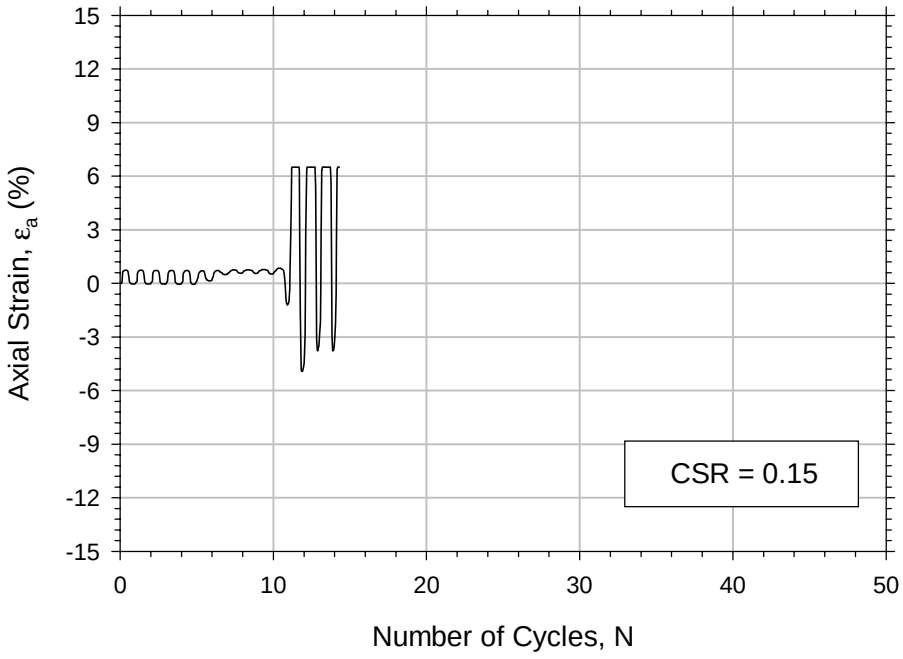

b) Axial Strain

Figure 3.7 Cyclic Triaxial Test Results for Loose Samples at CSR = 0.15

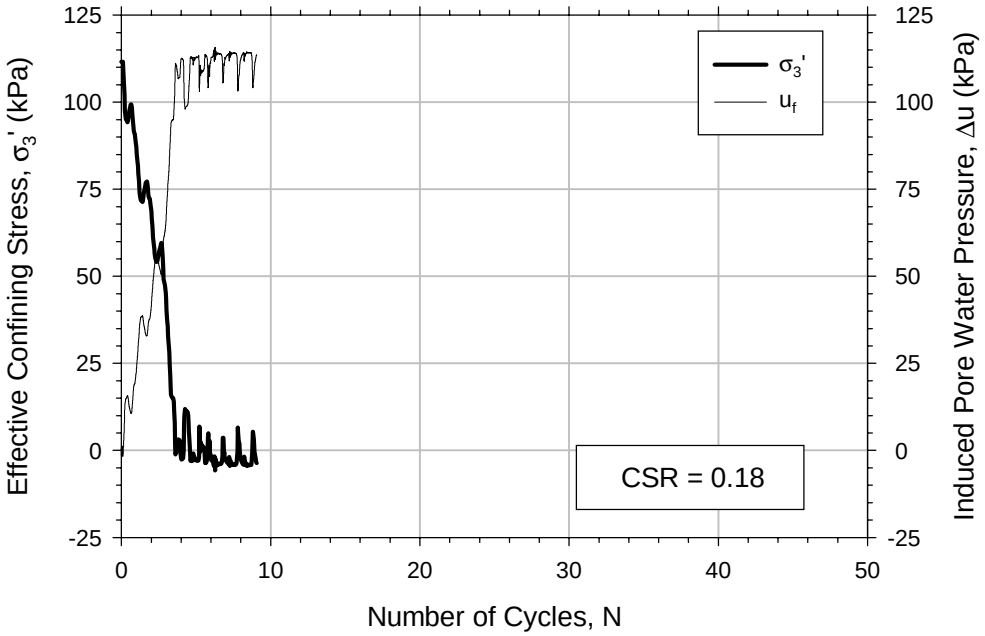

a) Effective Stress

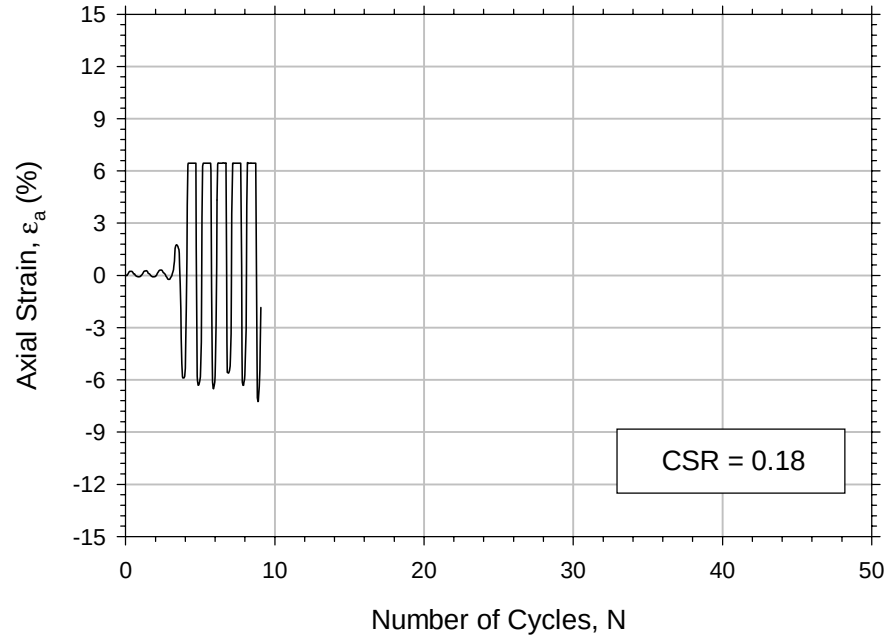

b) Axial Strain

Figure 3.8 Cyclic Triaxial Test Results for Loose Samples at CSR = 0.18

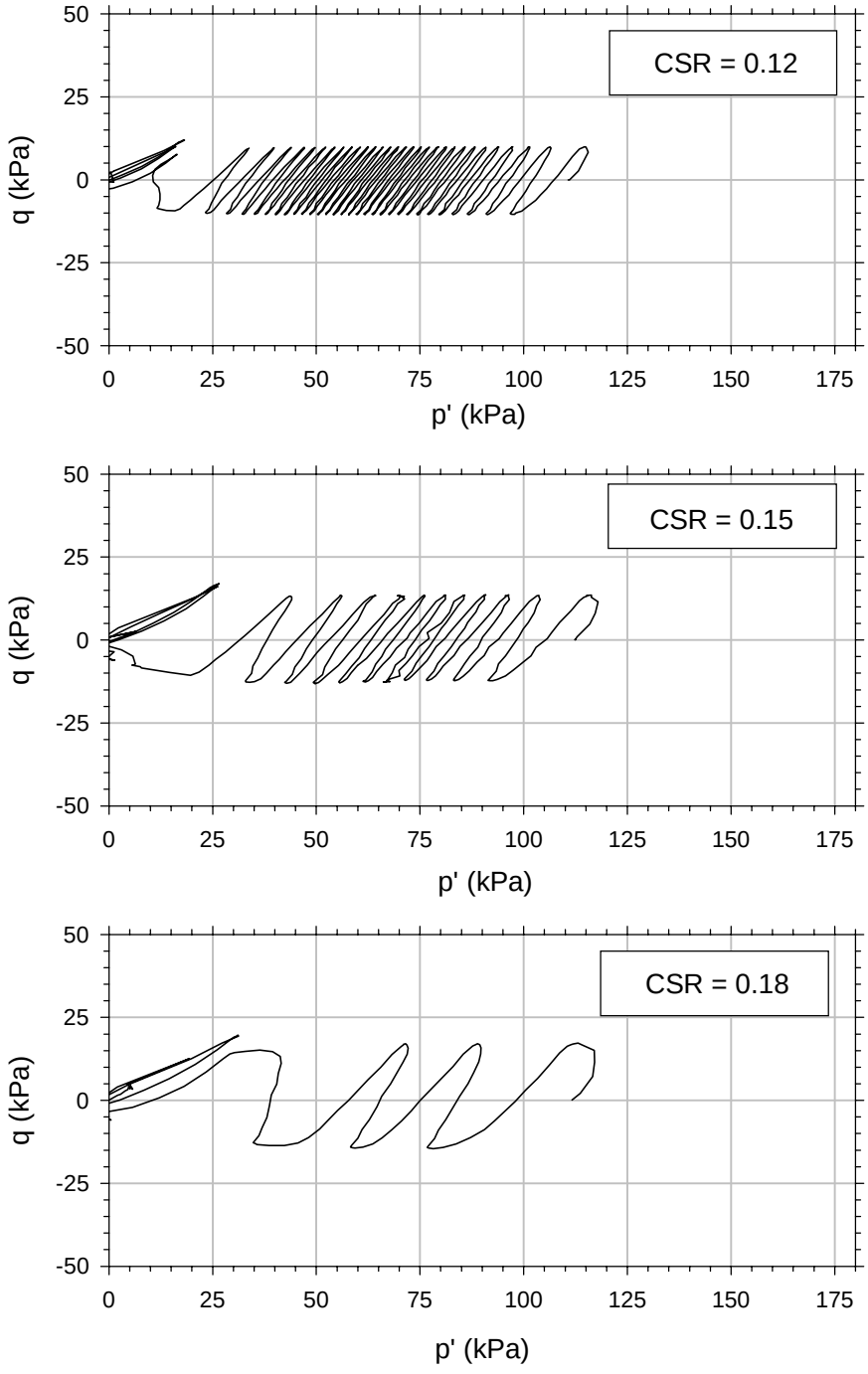

Figure 3.9 Stress Paths from Cyclic Triaxial Tests on Loose Samples

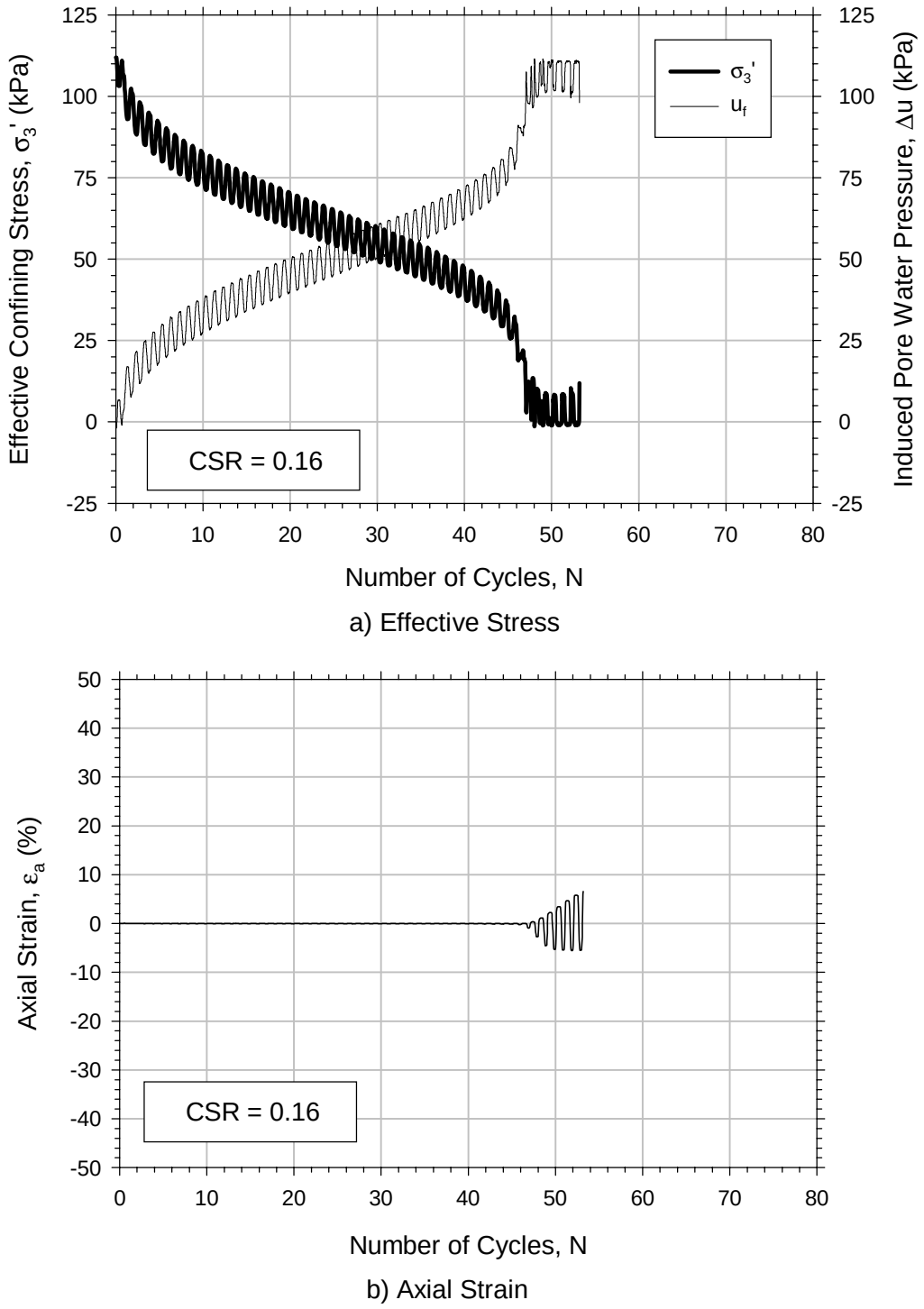

Figure 3.10 Cyclic Triaxial Test Results for Medium Dense Samples at CSR = 0.16

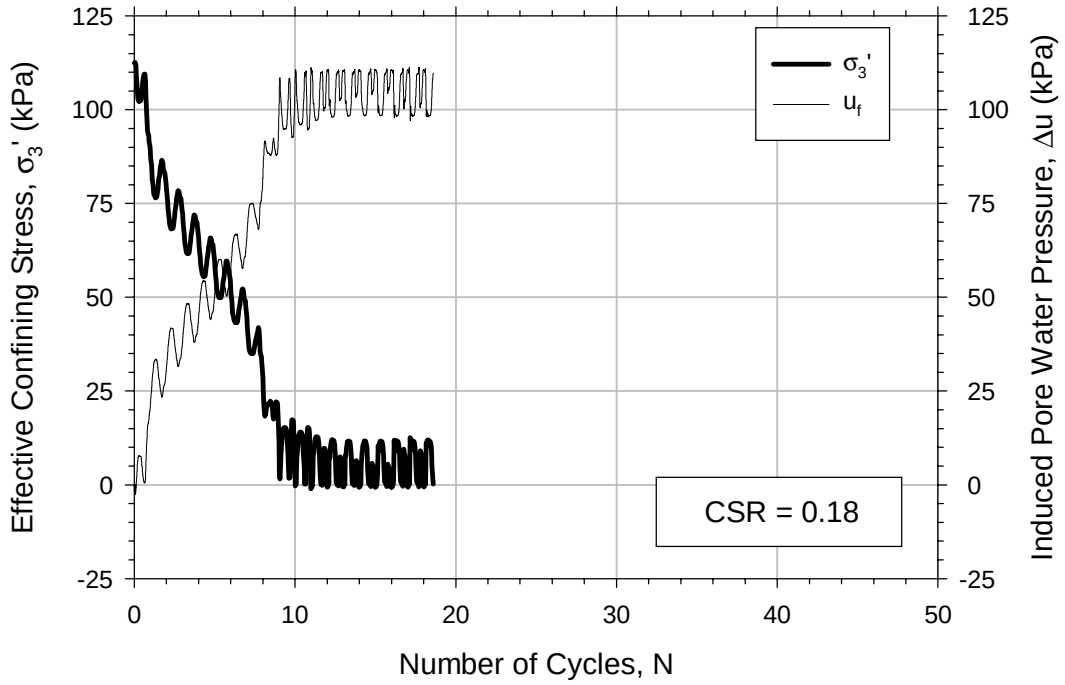

a) Effective Stress

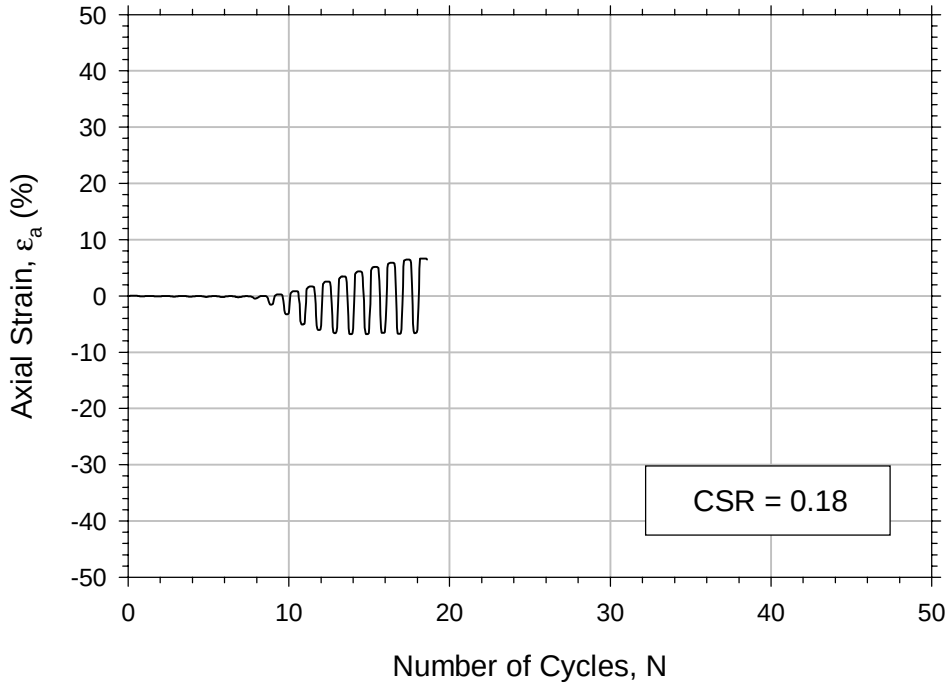

b) Axial Strain

Figure 3.11 Cyclic Triaxial Test Results for Medium Dense Samples at CSR = 0.18

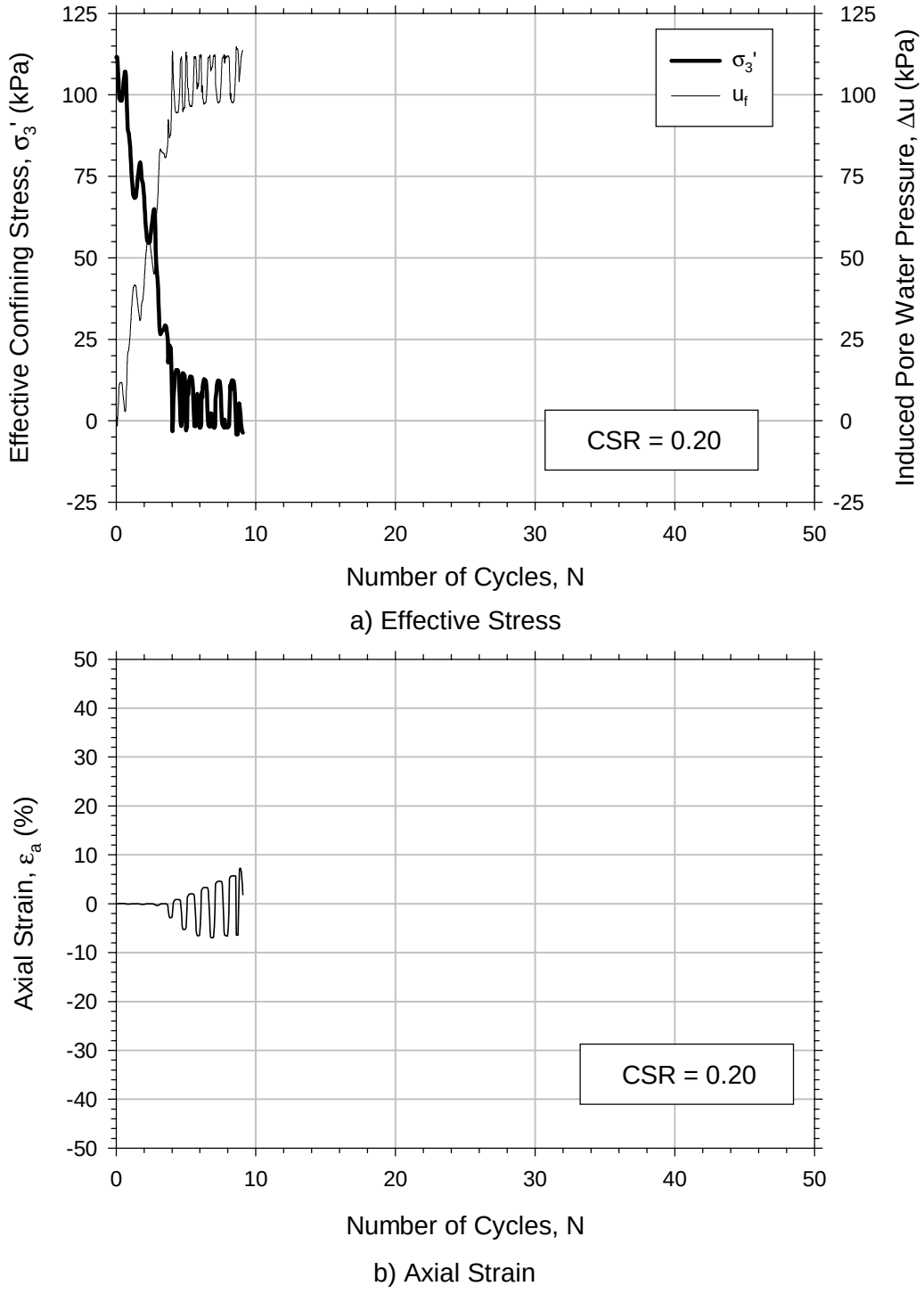

Figure 3.12 Cyclic Triaxial Test Results for Medium Dense Samples at CSR = 0.20

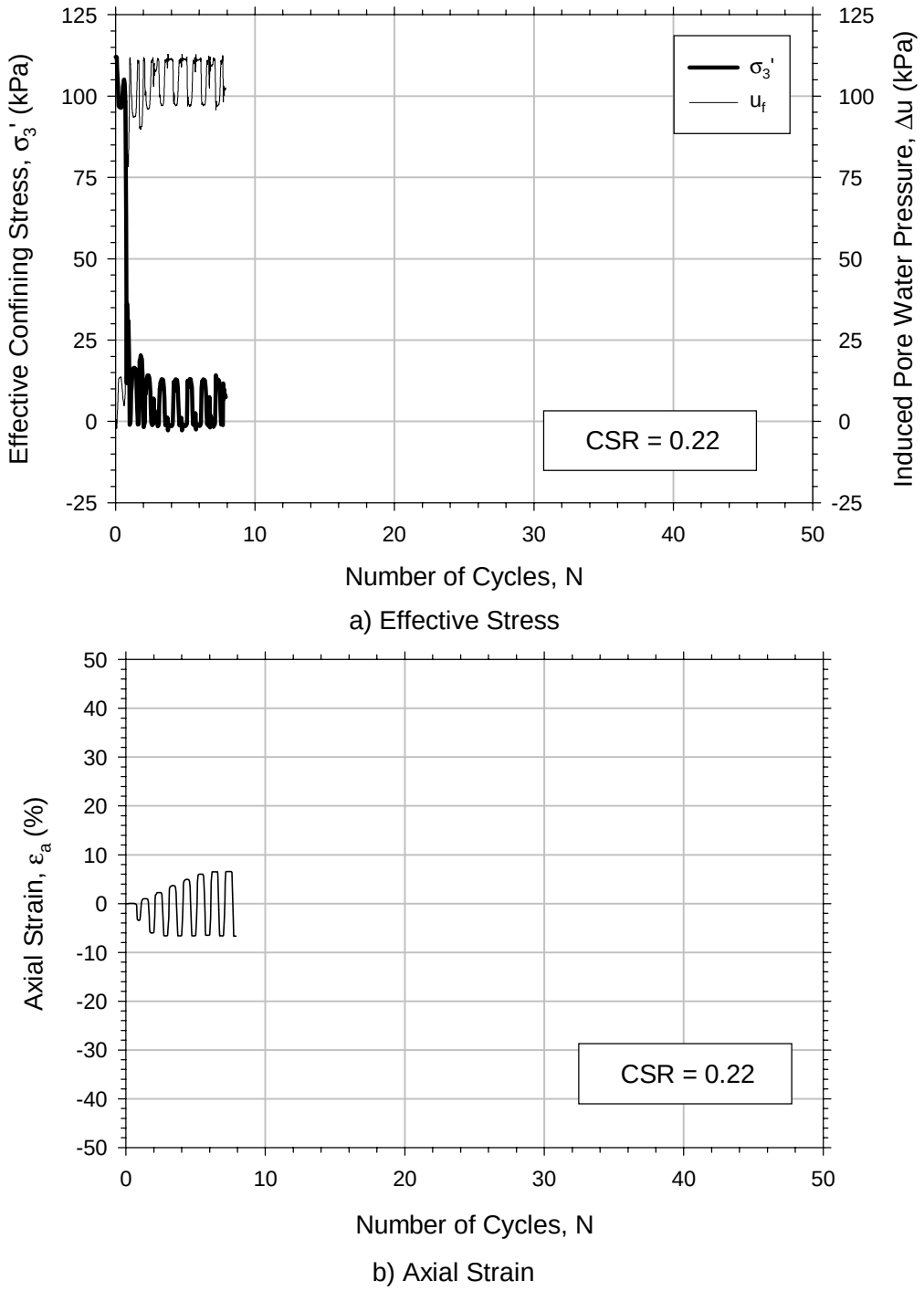

Figure 3.13 Cyclic Triaxial Test Results for Medium Dense Samples at CSR = 0.22

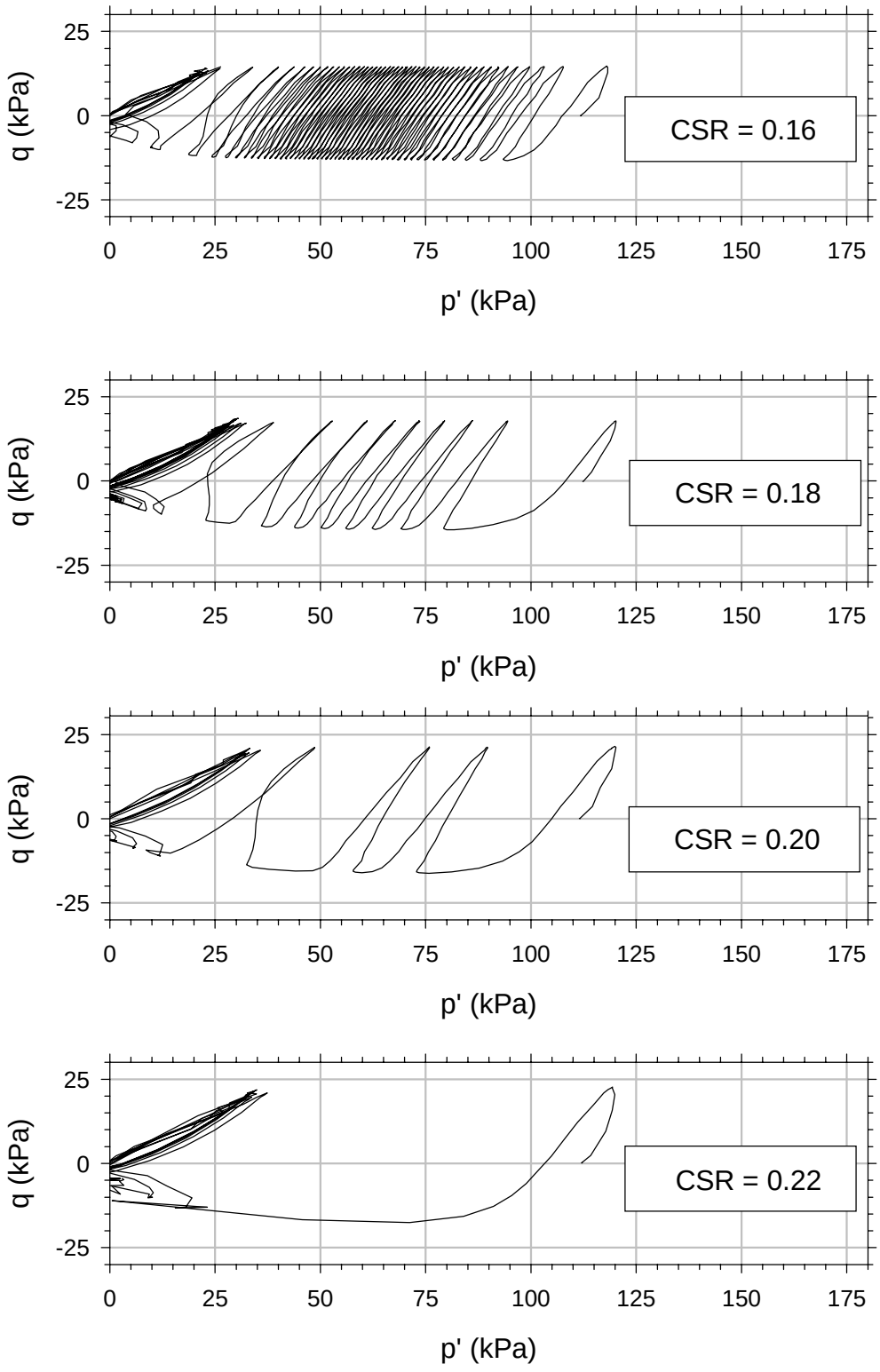

Figure 3.14 Stress Paths from Cyclic Triaxial Tests on Medium Dense Samples

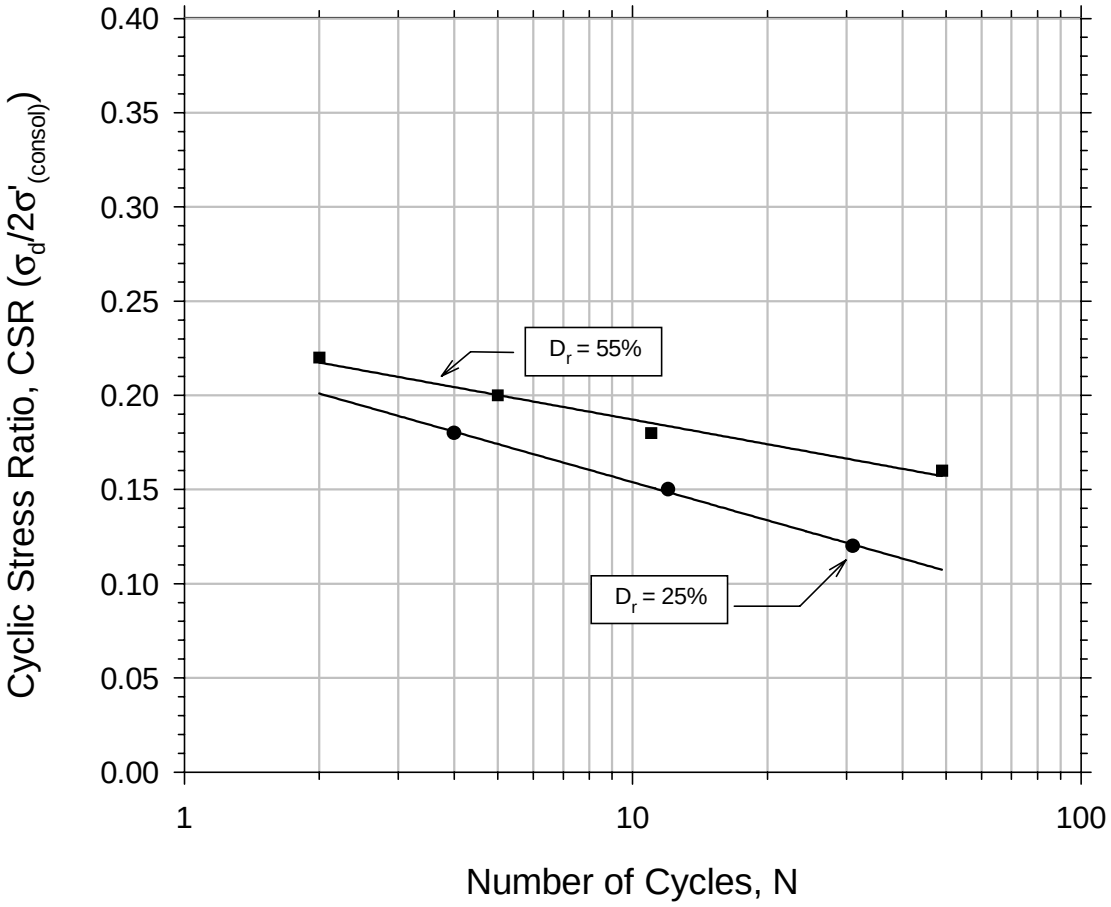

Figure 3.15 CSR vs. Number of Cycles to Failure for Loose and Medium Dense Soils

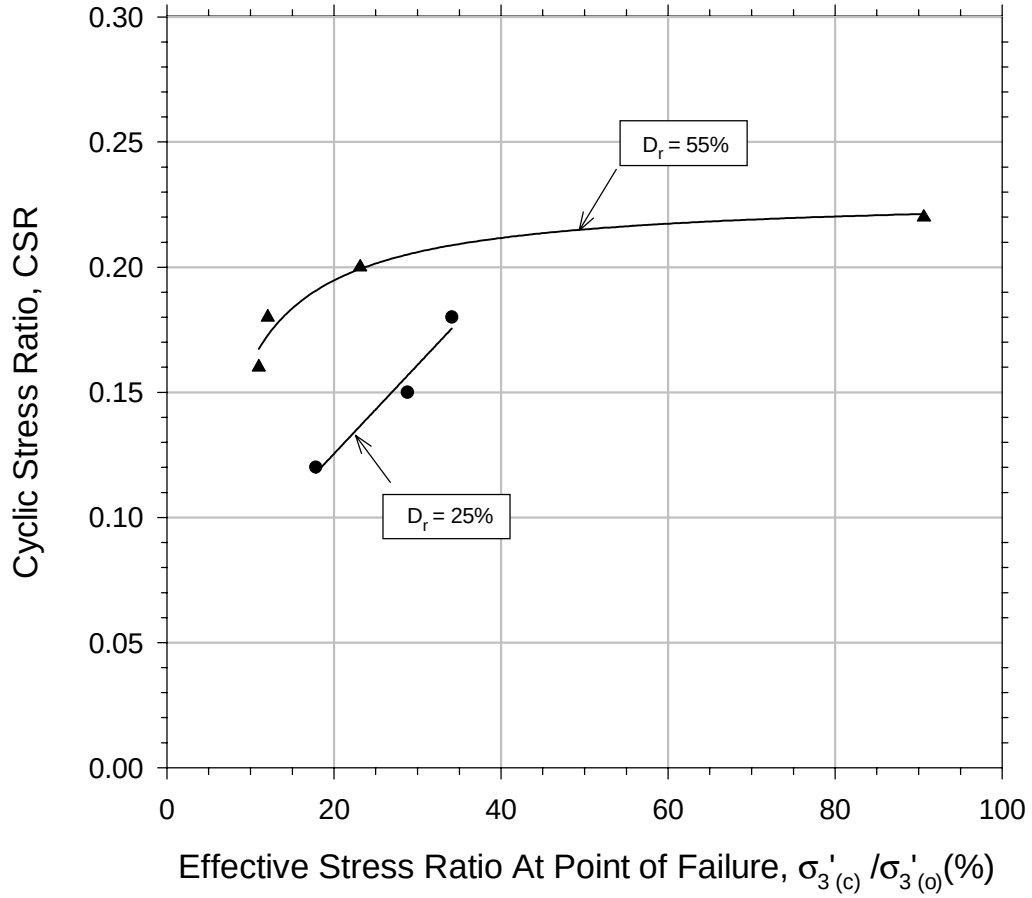

Figure 3.16 Comparison of the Effective Stress in the Soil at the Point of Failure

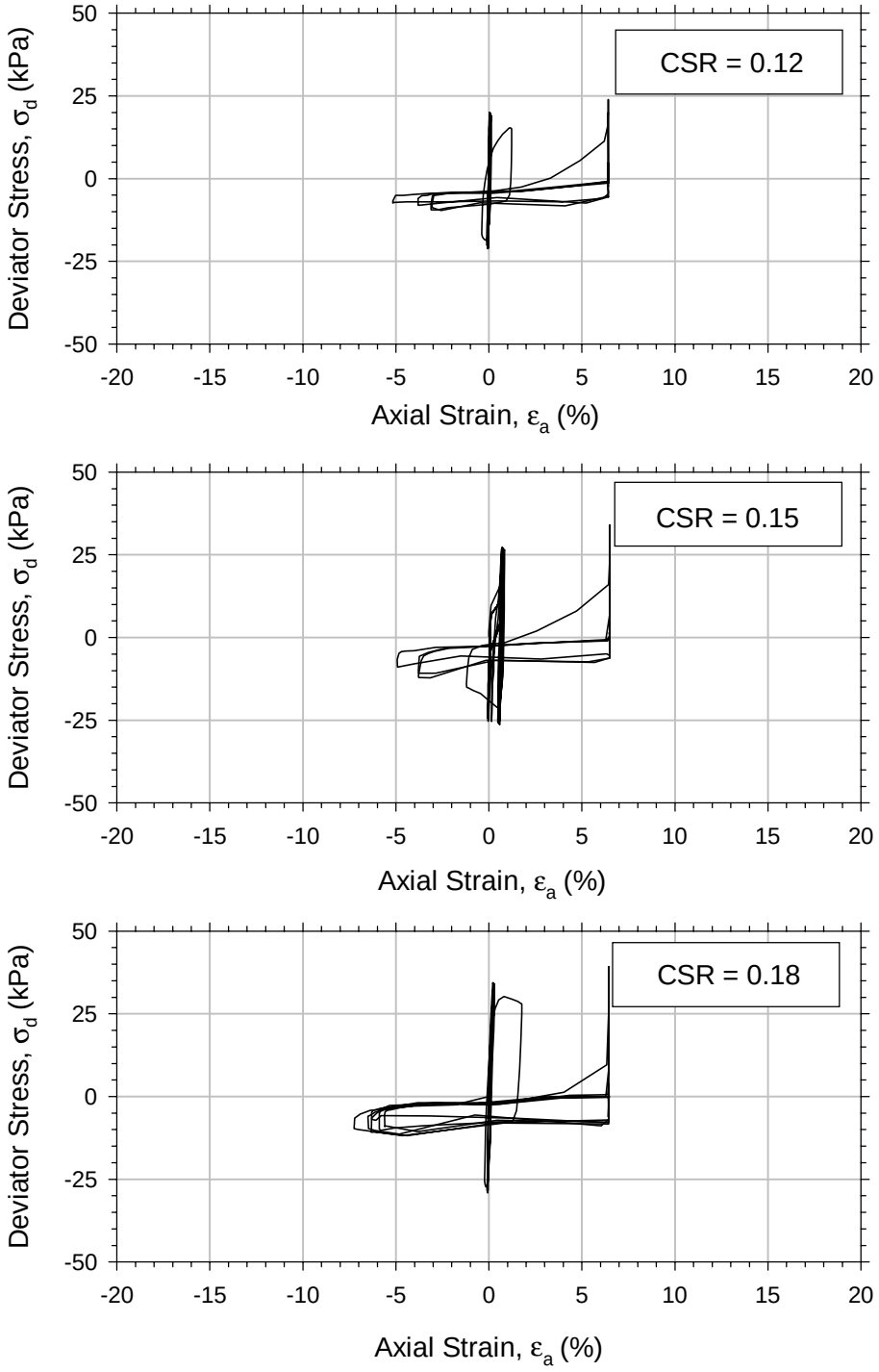

Figure 3.17 Hysteresis Loops from Triaxial Tests on Loose Samples

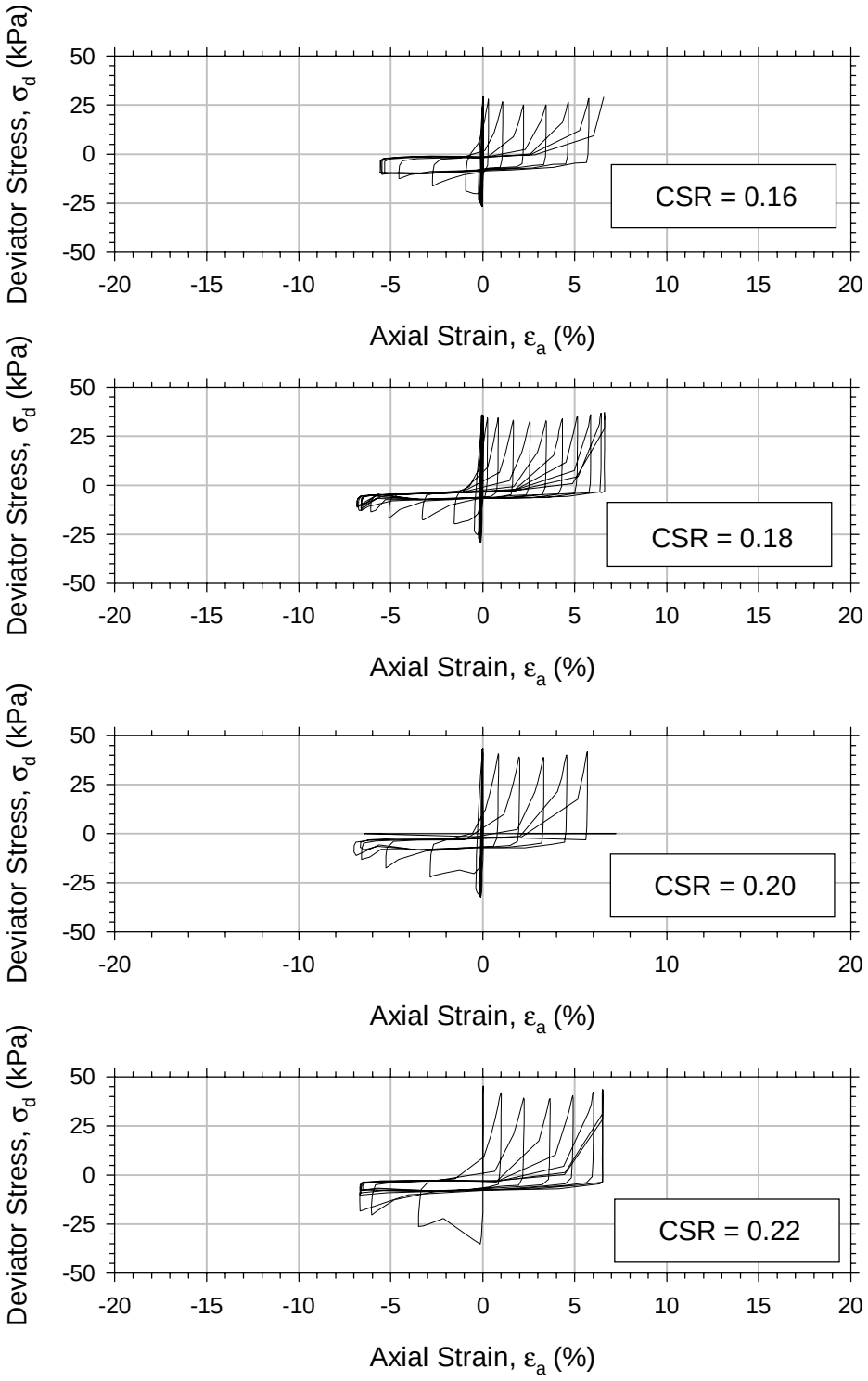

Figure 3.18 Hysteresis Loops from Triaxial Tests on Medium Dense Samples

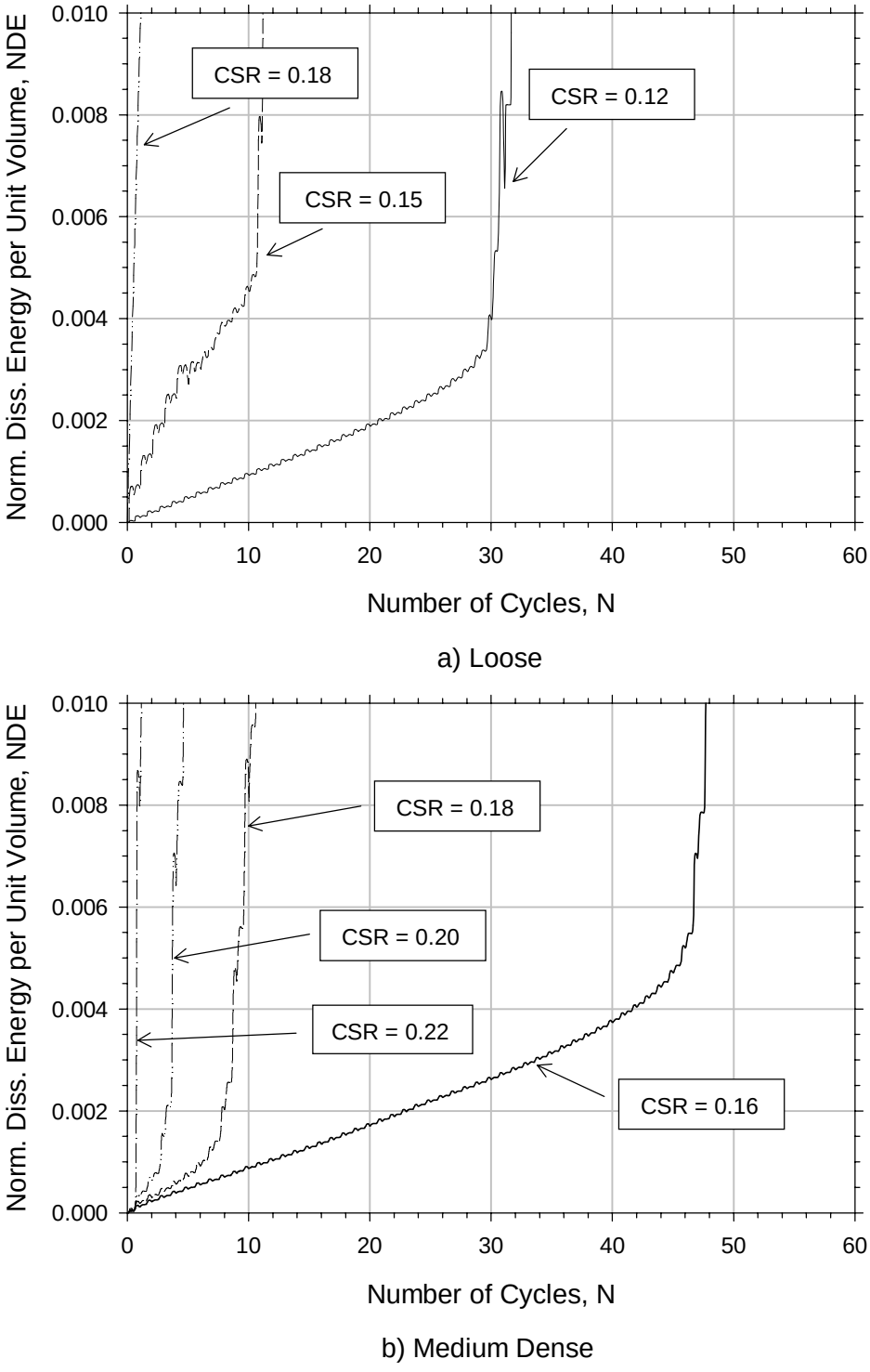

Figure 3.19 NDE as a Function of the Number of Cycles of Loading

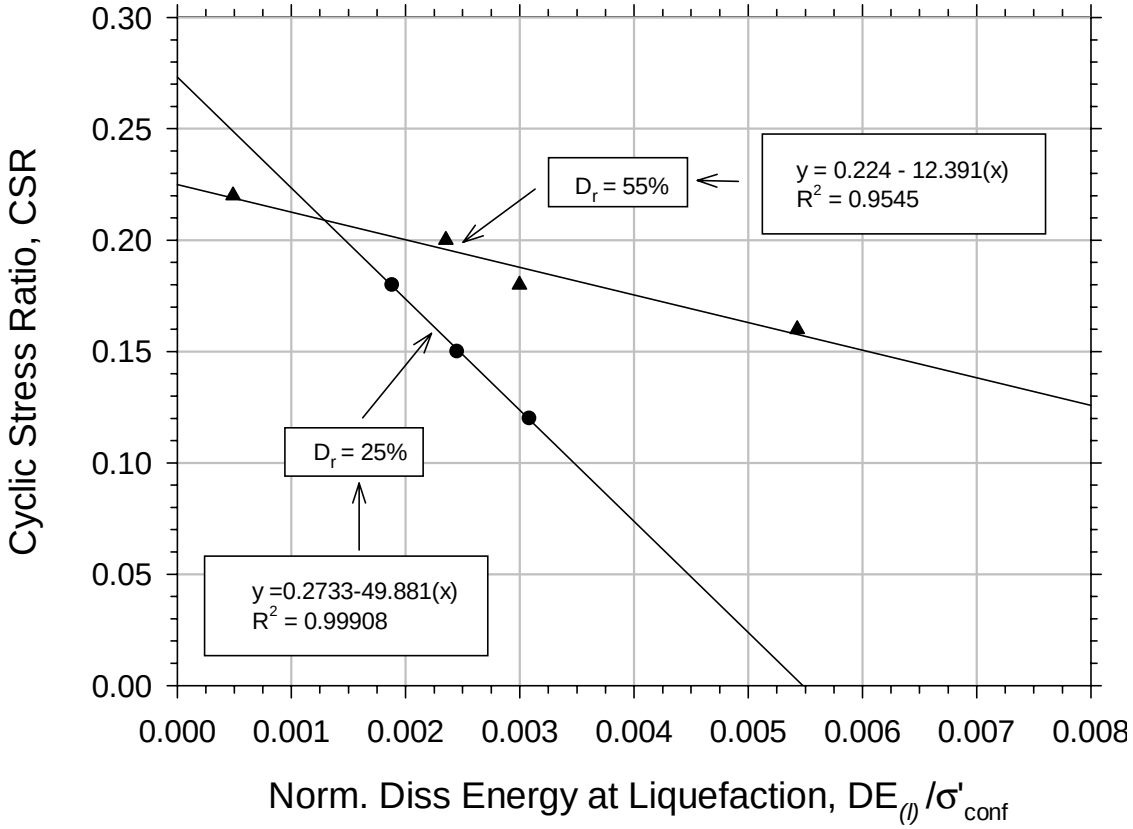

Figure 3.20 NDE at the Point of Liquefaction for Different CSR

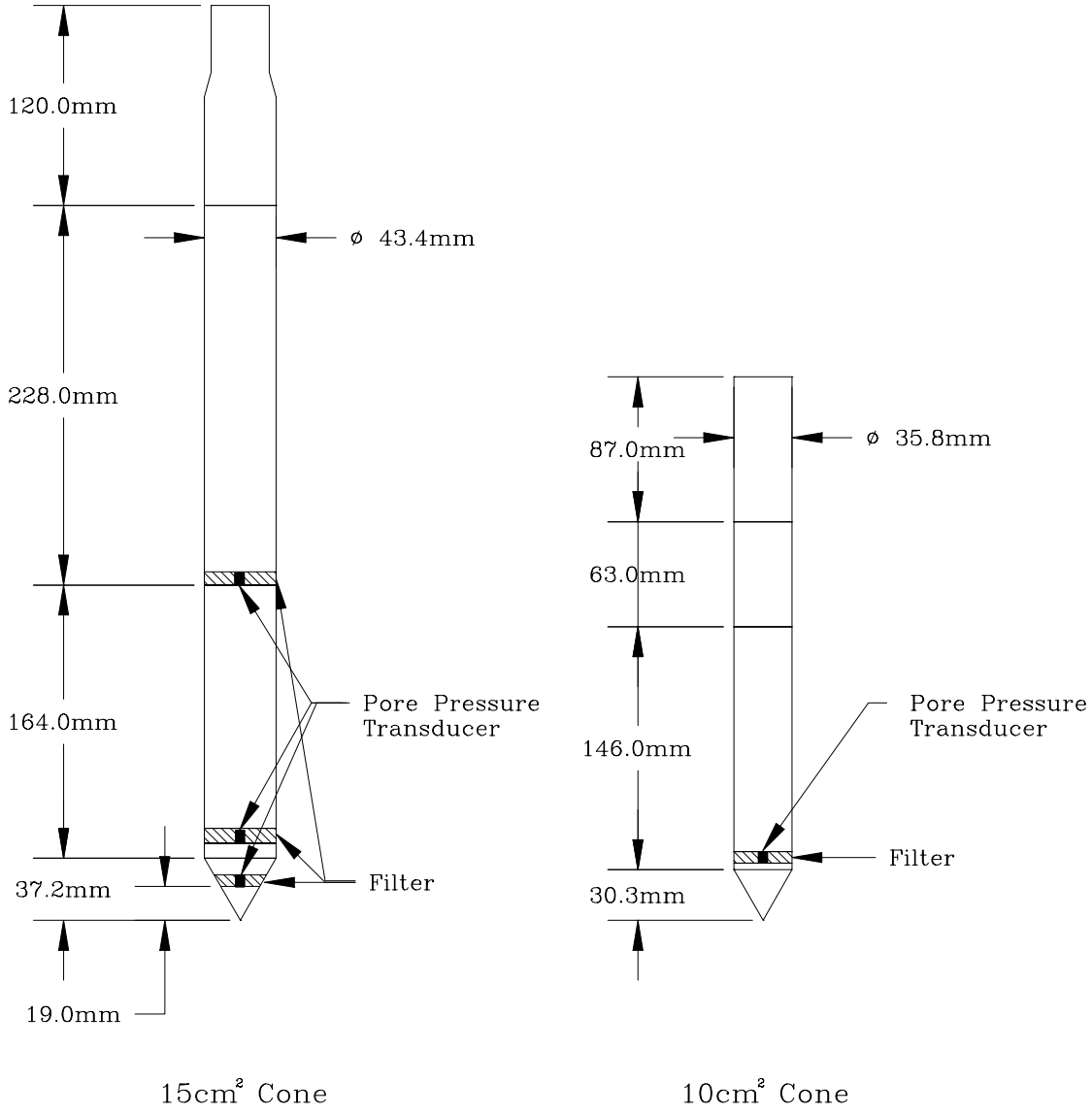

Figure 3.21 Schematics of 15-cm^2 and 10-cm^2 Cone Penetrometers Used in Testing

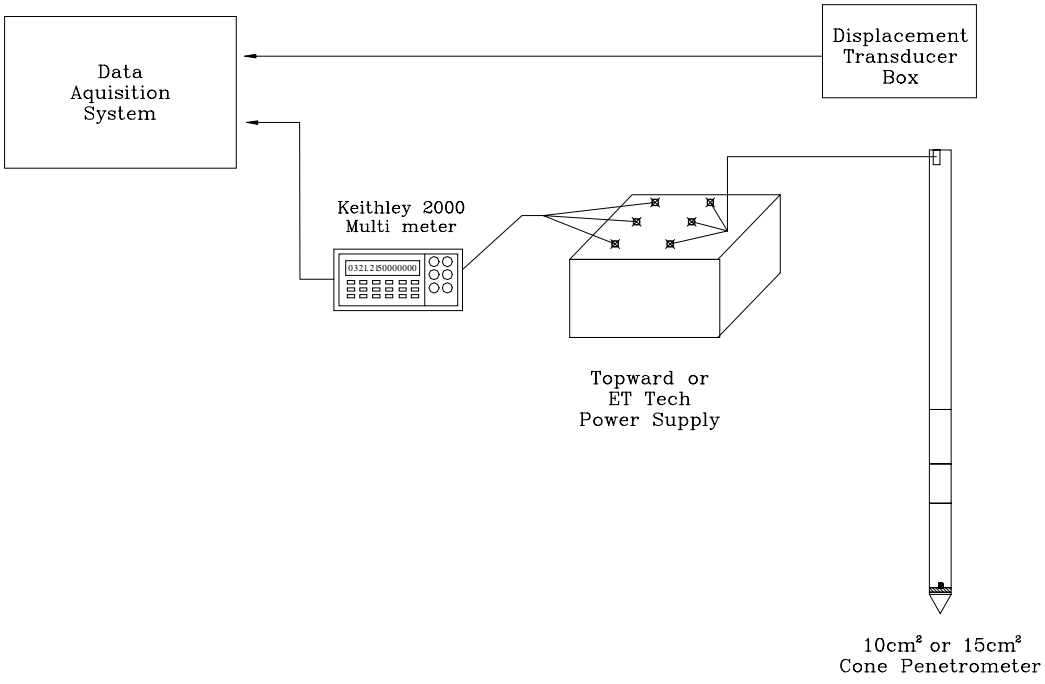

Figure 3.22 Schematic of Cone Penetration System Used in Calibration Chamber Testing

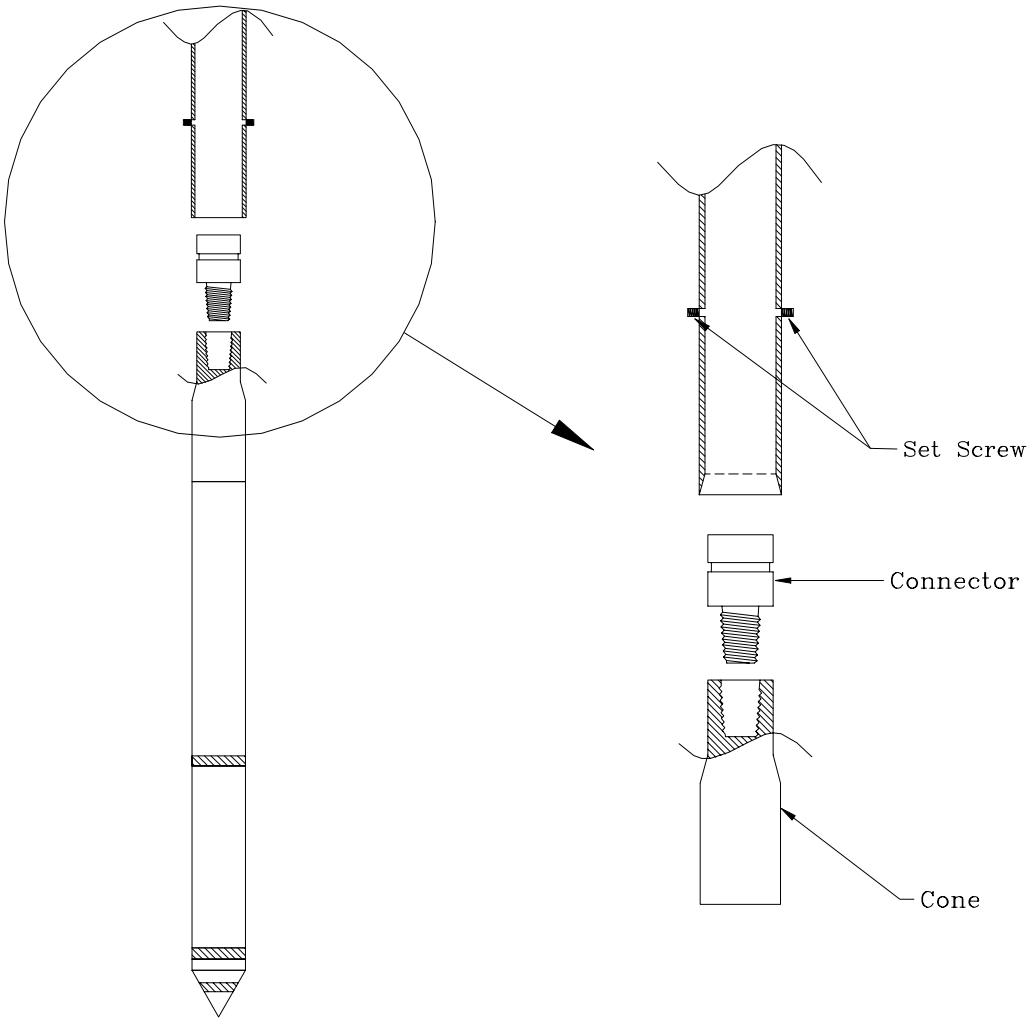

Figure 3.23 Drill Rod and Connecting Fitting for 15-cm^2 Cone

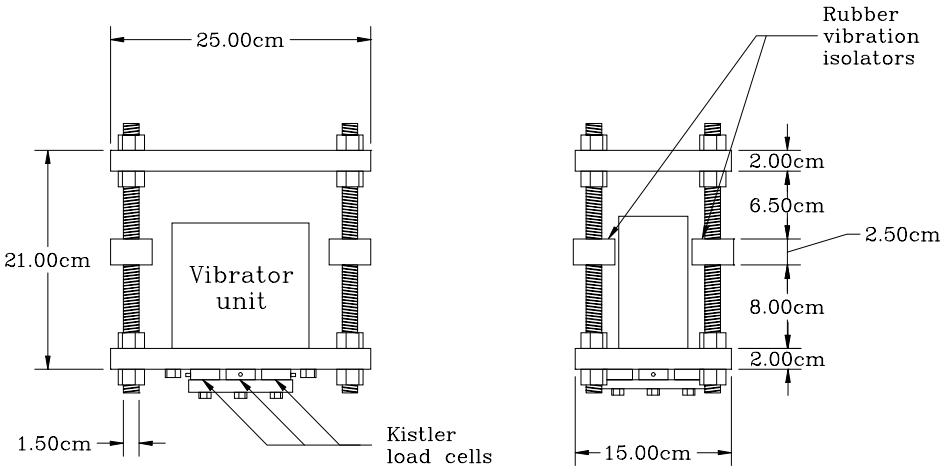

a) Vibrator Housing and Load Cells

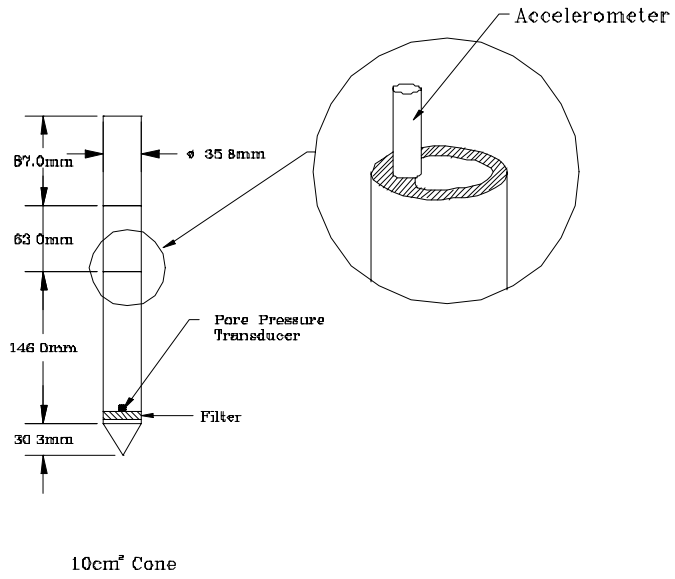

b) Accelerometer Location

Figure 3.24 Schematic of Vibration Monitoring Devices

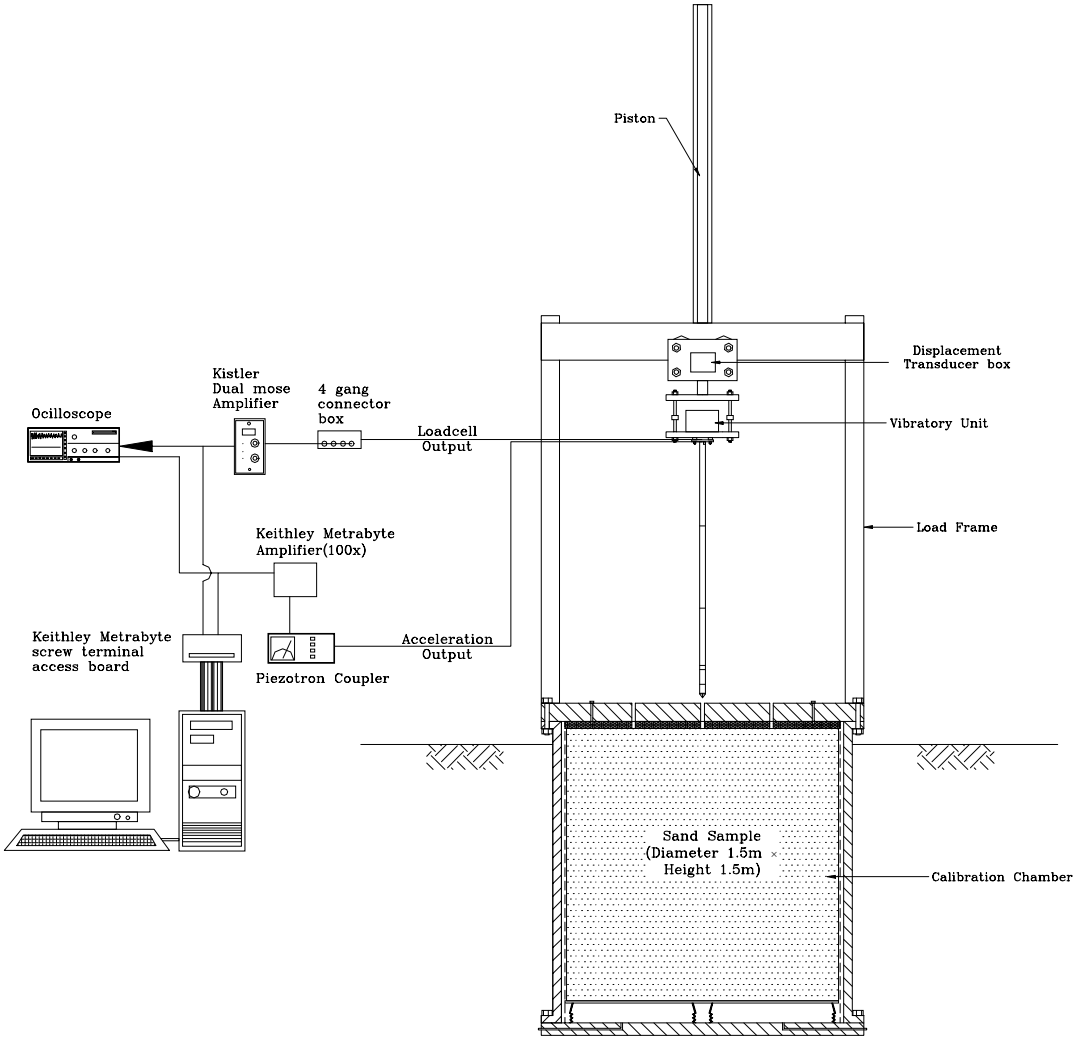

Figure 3.25 Schematic of Vibration Monitoring System

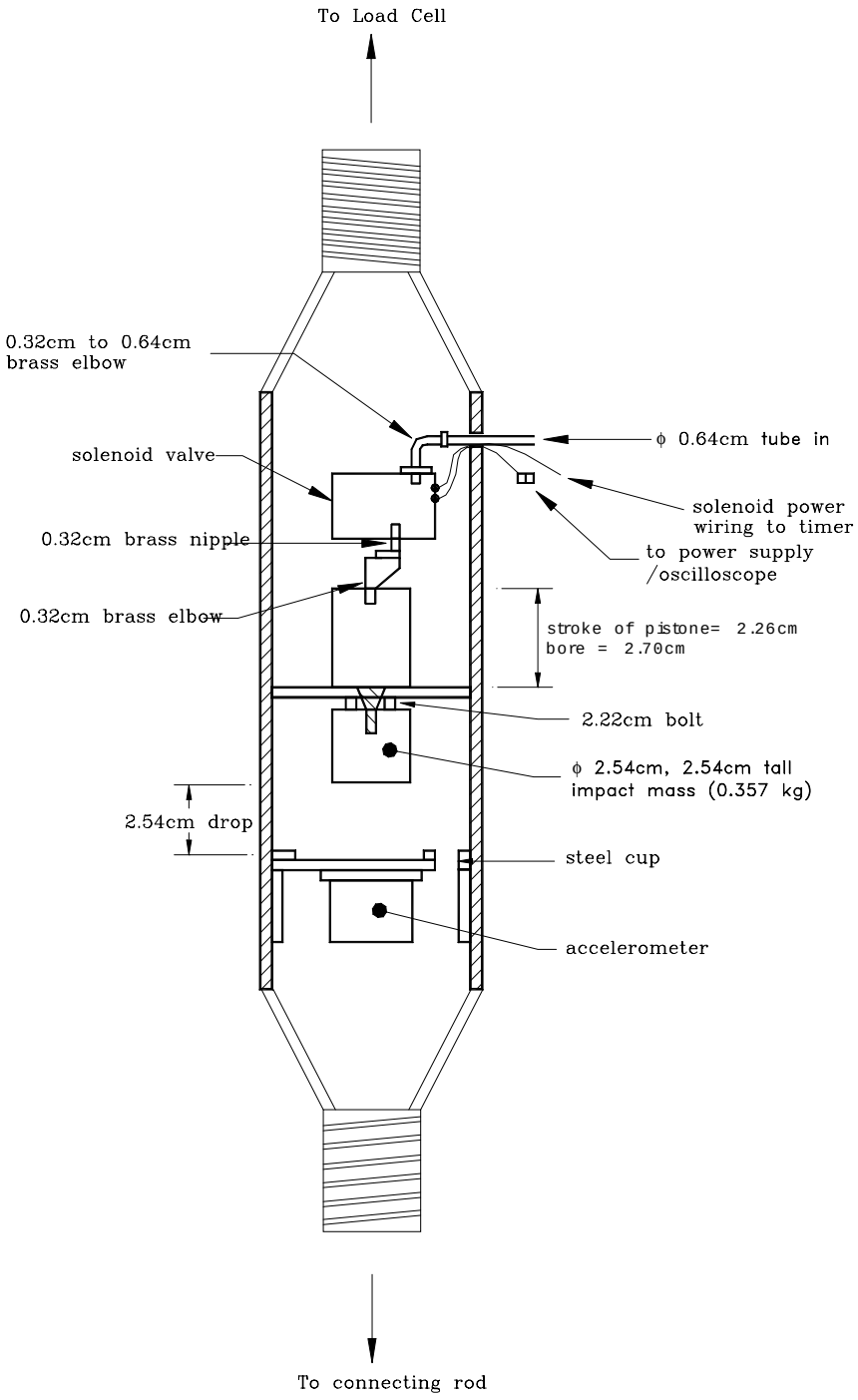

Figure 3.26 Schematic of Pneumatic Impact Vibrator

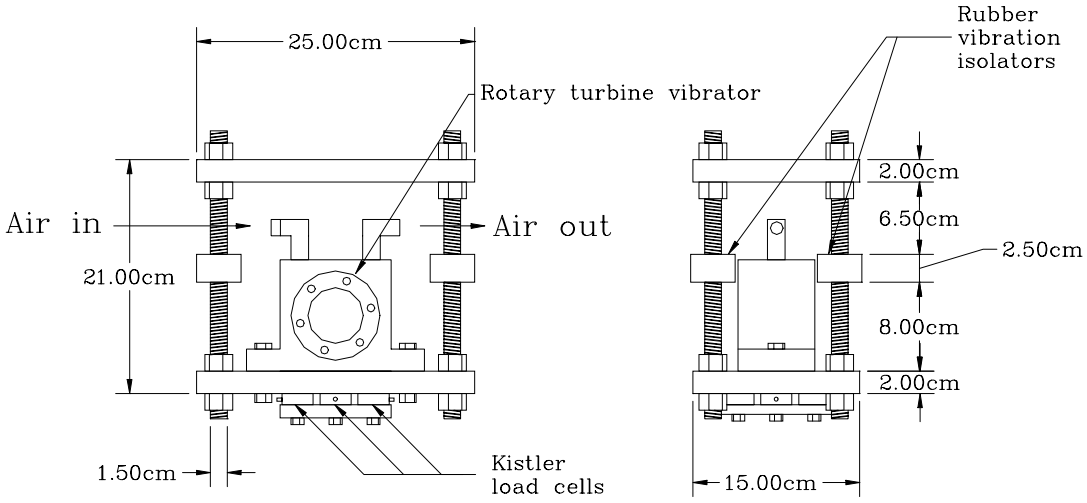

Figure 3.27 Schematic of Rotary Turbine Vibrator

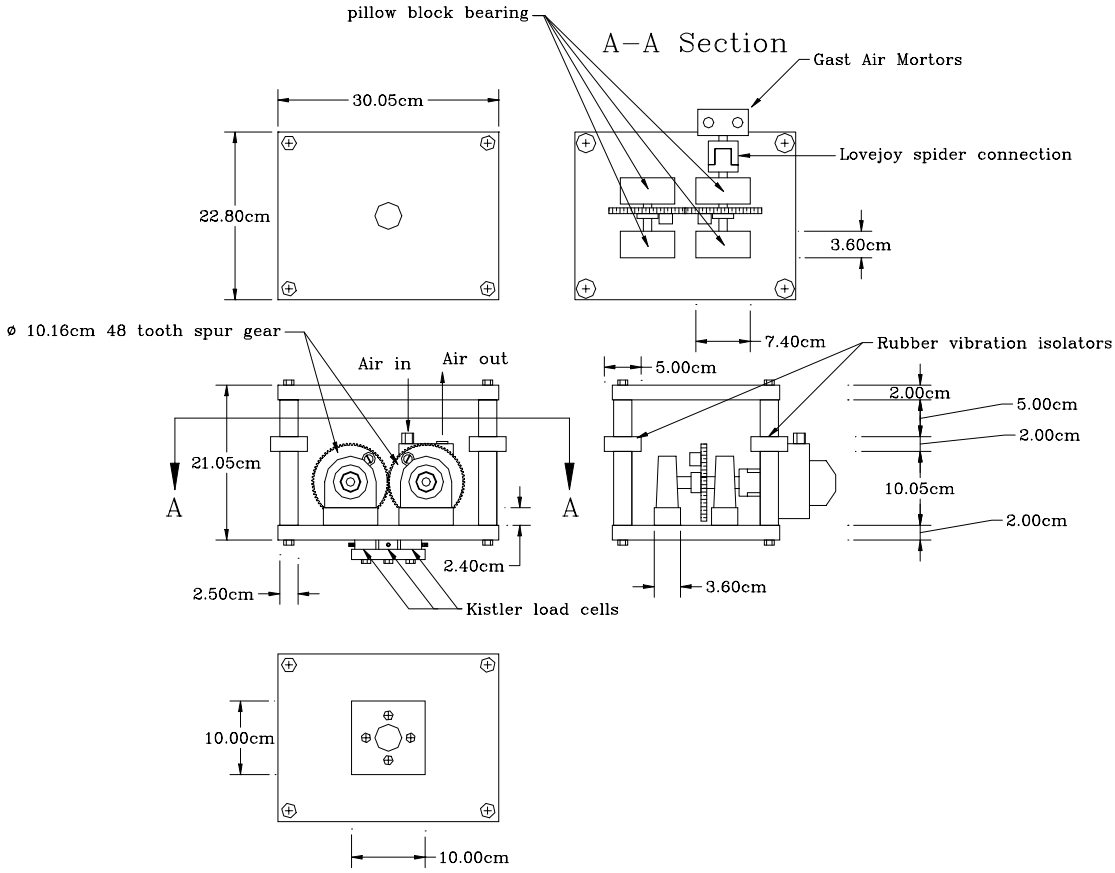

Figure 3.28 Schematic of Counter Rotating Mass Vibrator

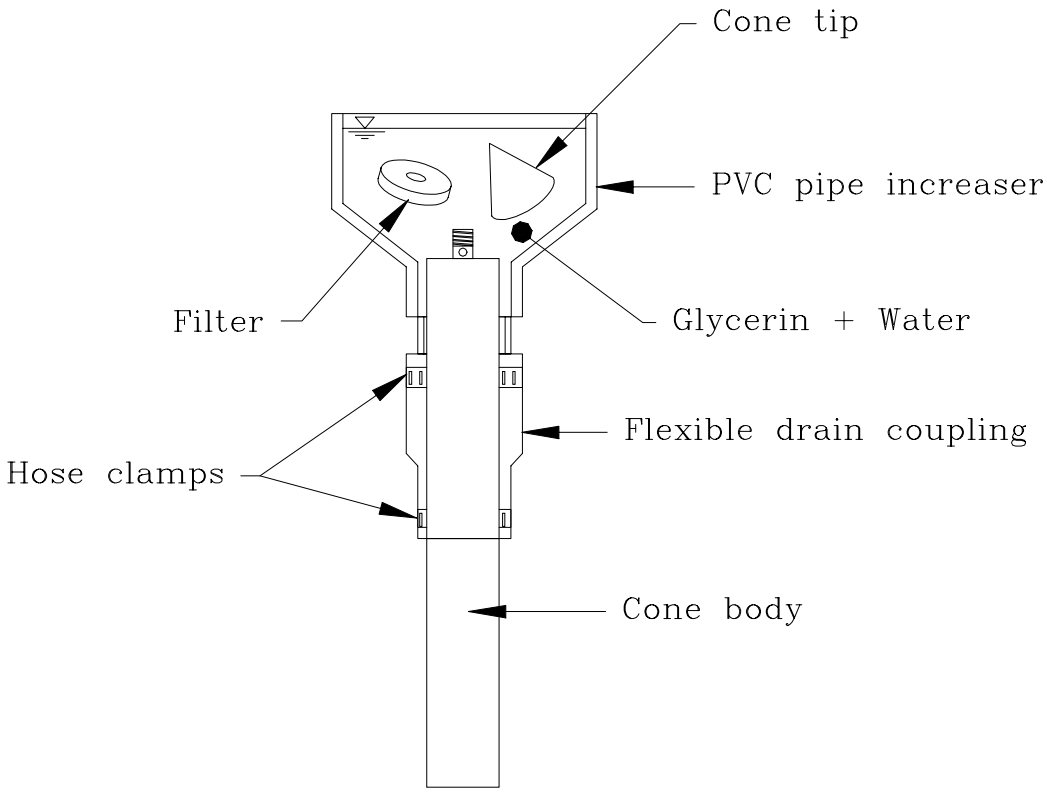

Figure 3.29 Schematic of Saturation Apparatus

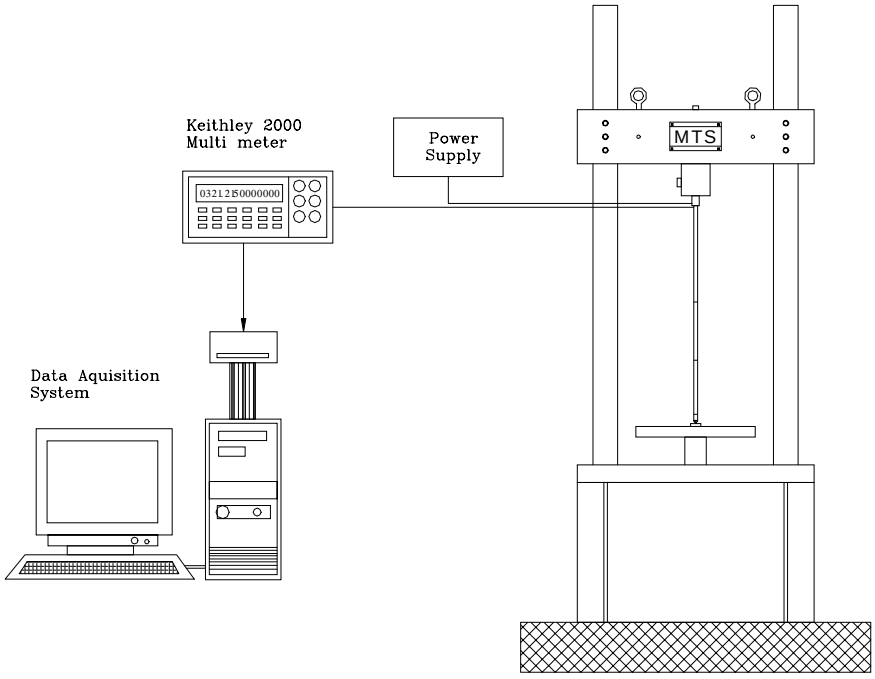

a) Load Cell Calibration

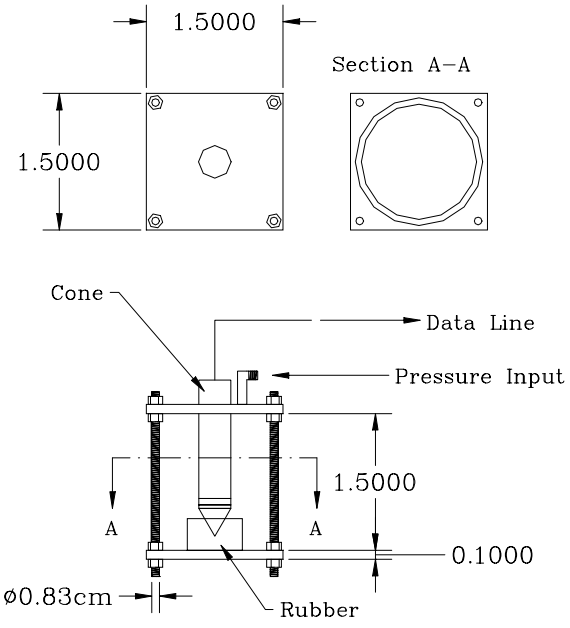

b) Pore Pressure Transducer Calibration

Figure 3.30 Setup Used to Calibrate Cone Penetrometer Load Cells and Transducers

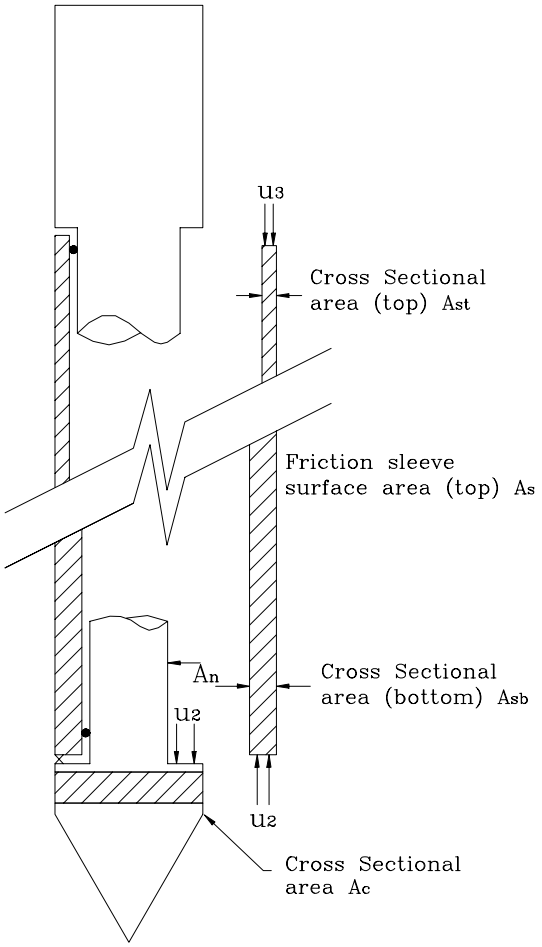

Figure 3.31 Unequal End Area Effects in Cone Penetrometer (After Lunne et al. 1997)

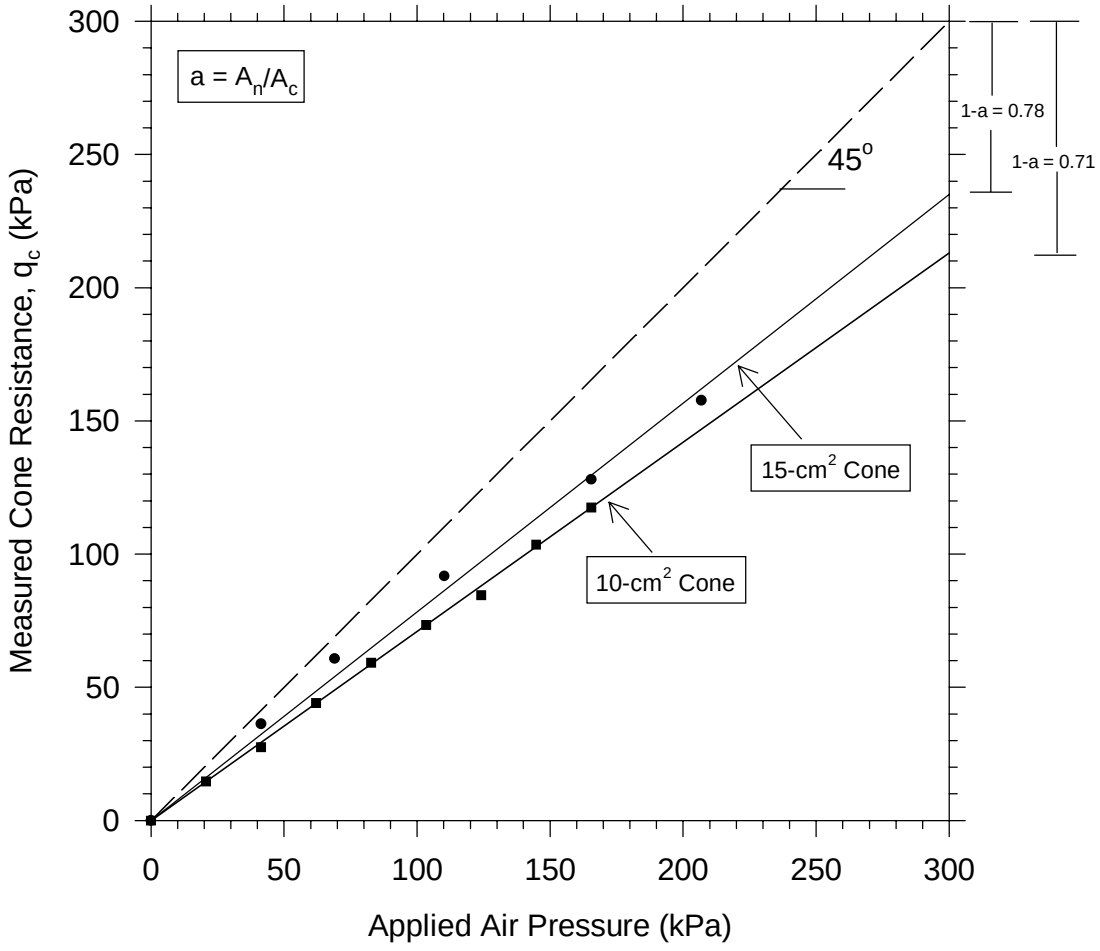

Figure 3.32 Calibration Curve Used to Determine Magnitude of Unequal End Area Effects

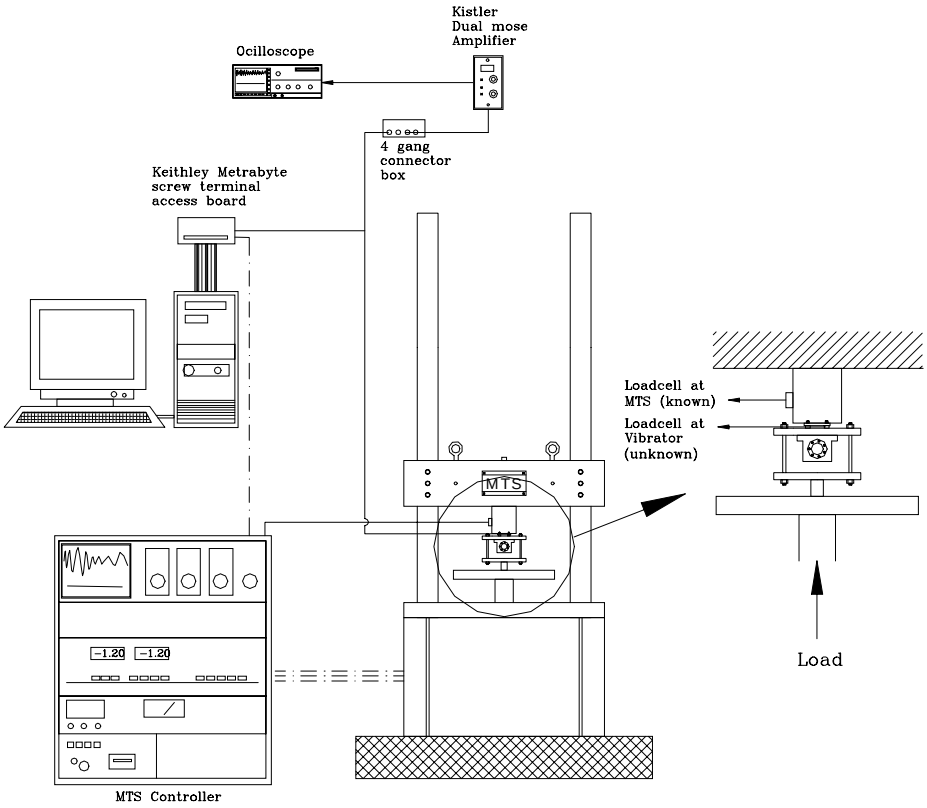

a) Load Cell Calibration Setup

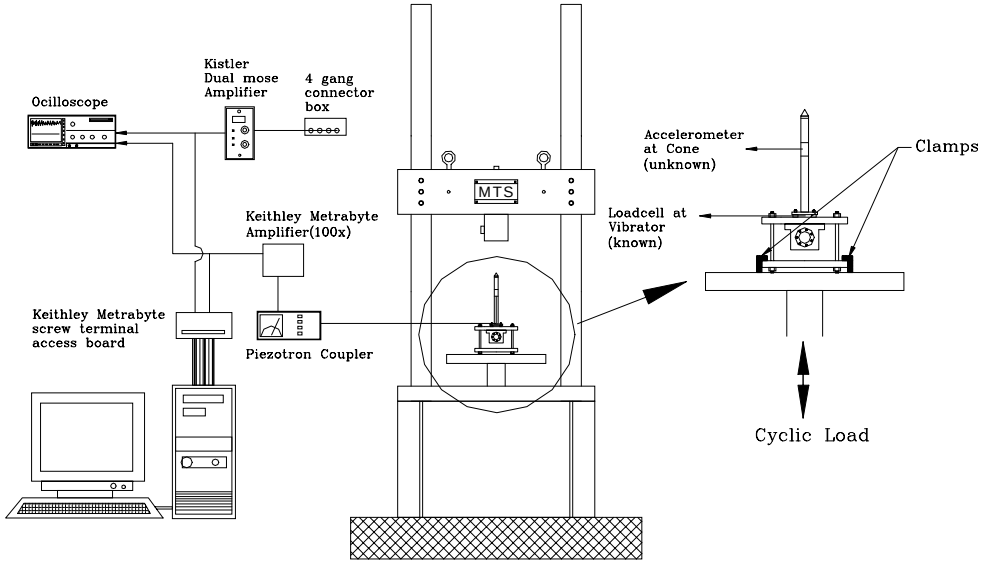

b) Accelerometer Calibration Setup

Figure 3.33 Schematic of Calibration Systems for Load Cells and Accelerometer

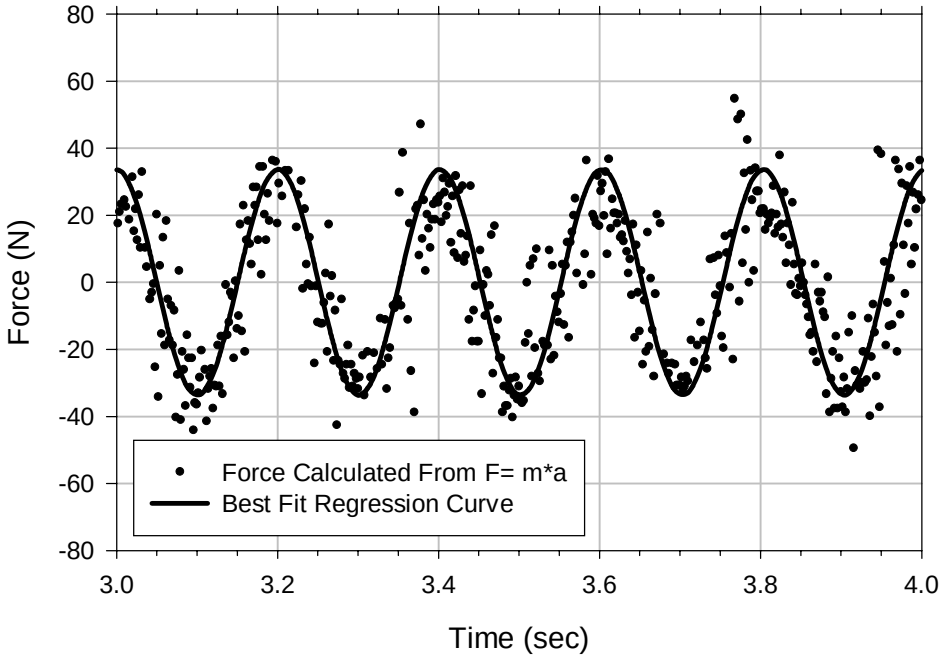

a) Estimated Force and Regression Curve

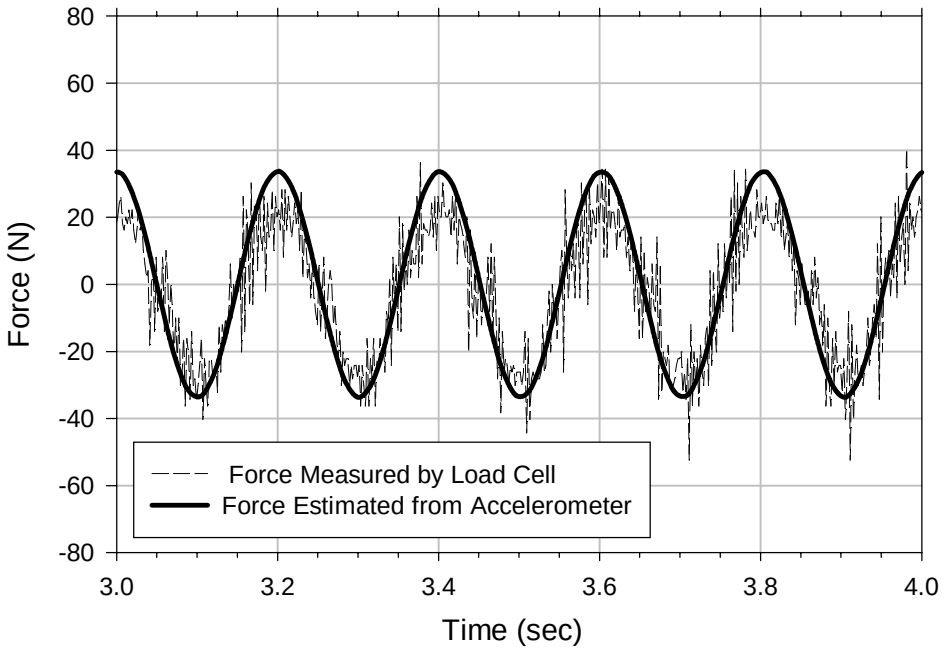

b) Measured Force at Load Cell and Estimated Force from Accelerometer

Figure 3.34 Verification of Manufacturers Calibration Factor for the Kistler 8602A500 Accelerometer

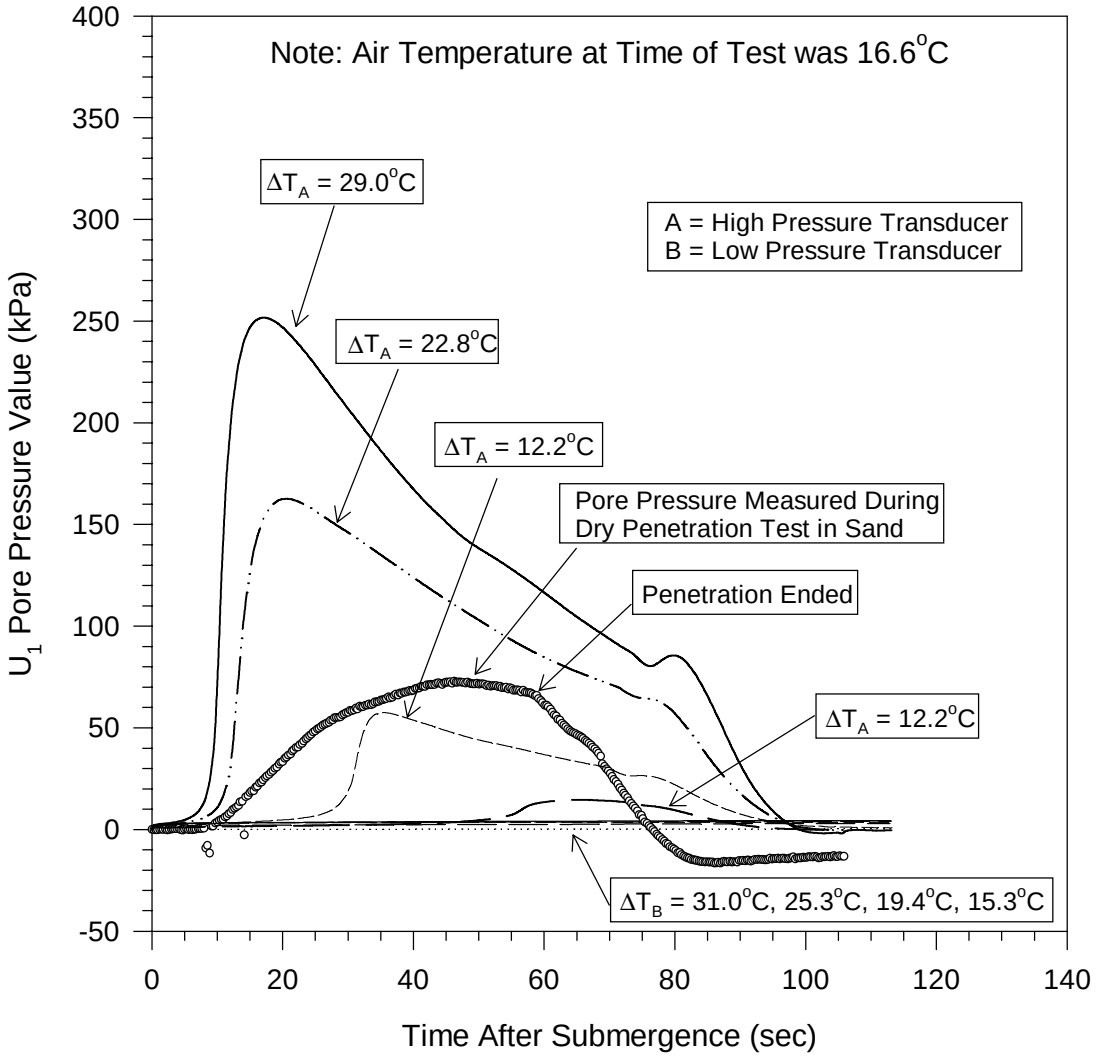

Figure 3.35 Submergence Test Results for 15-cm^2 Cone with High Pressure Transducers at the U_1 and U_2 locations

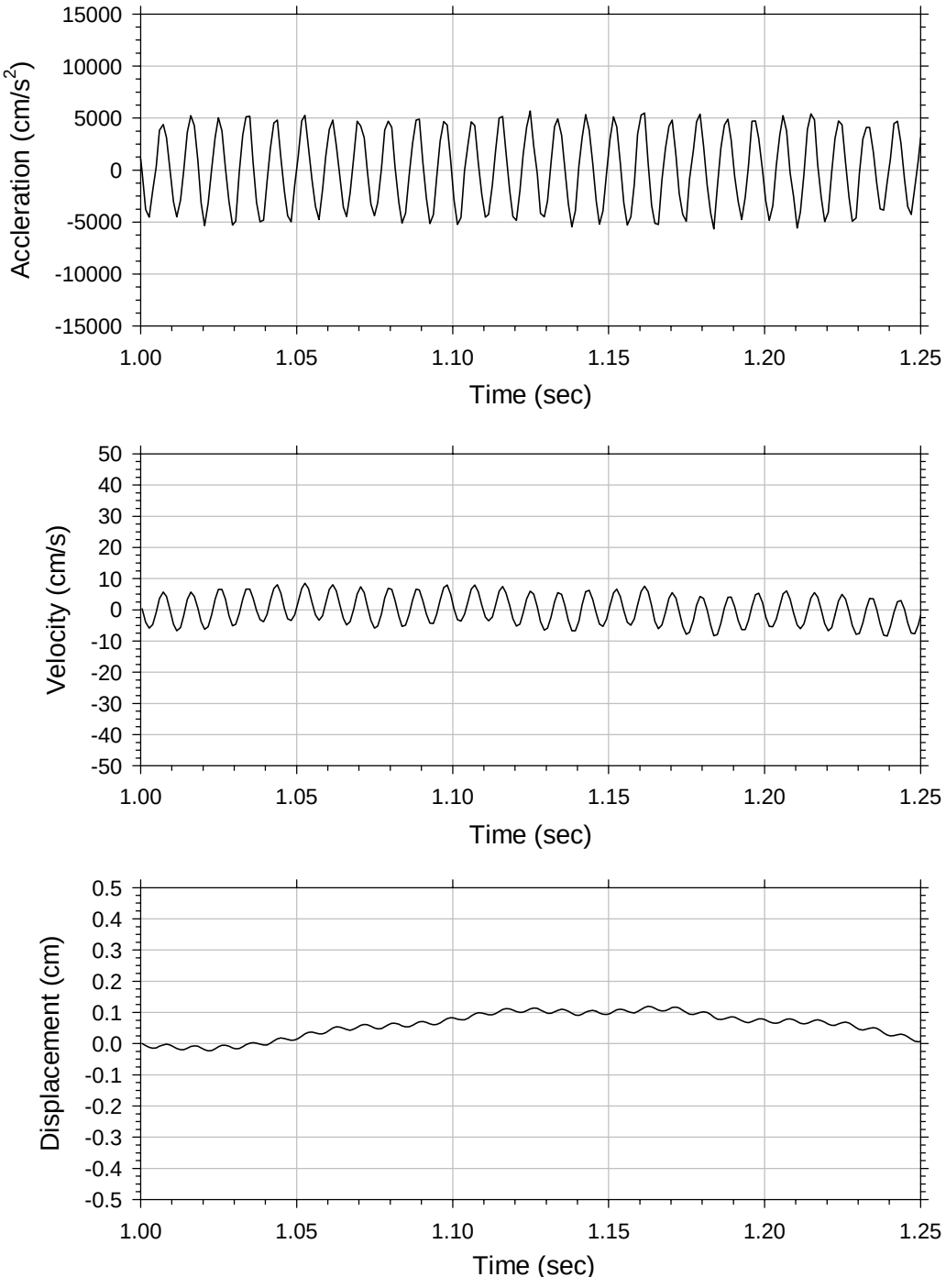

Figure 3.36 Representative Acceleration, Velocity, and Displacement Measured During Penetration at the Accelerometer Location Using Rotary Turbine Vibrator

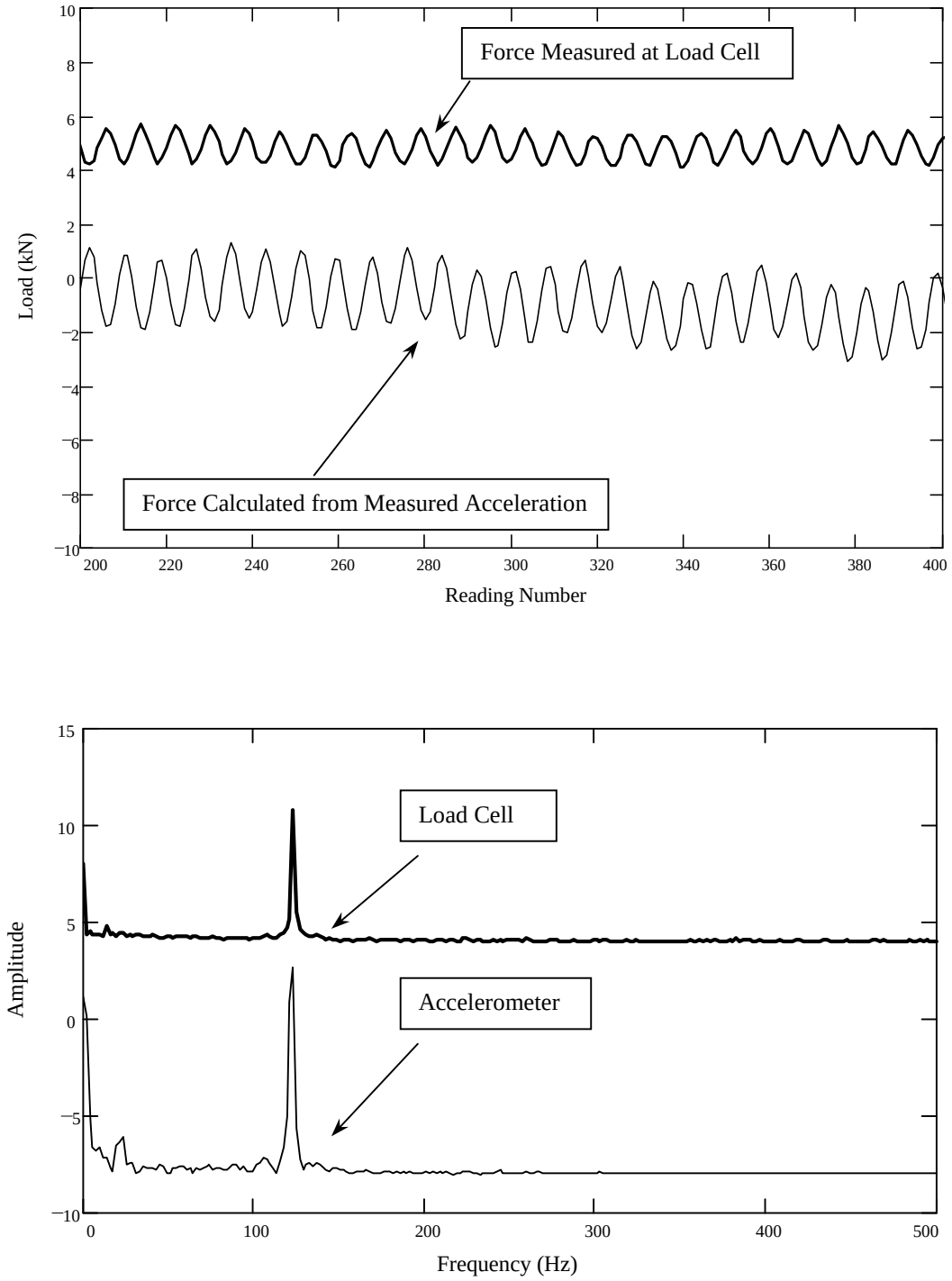

Figure 3.37 Representative Motion Generated by Rotary Turbine Vibrator

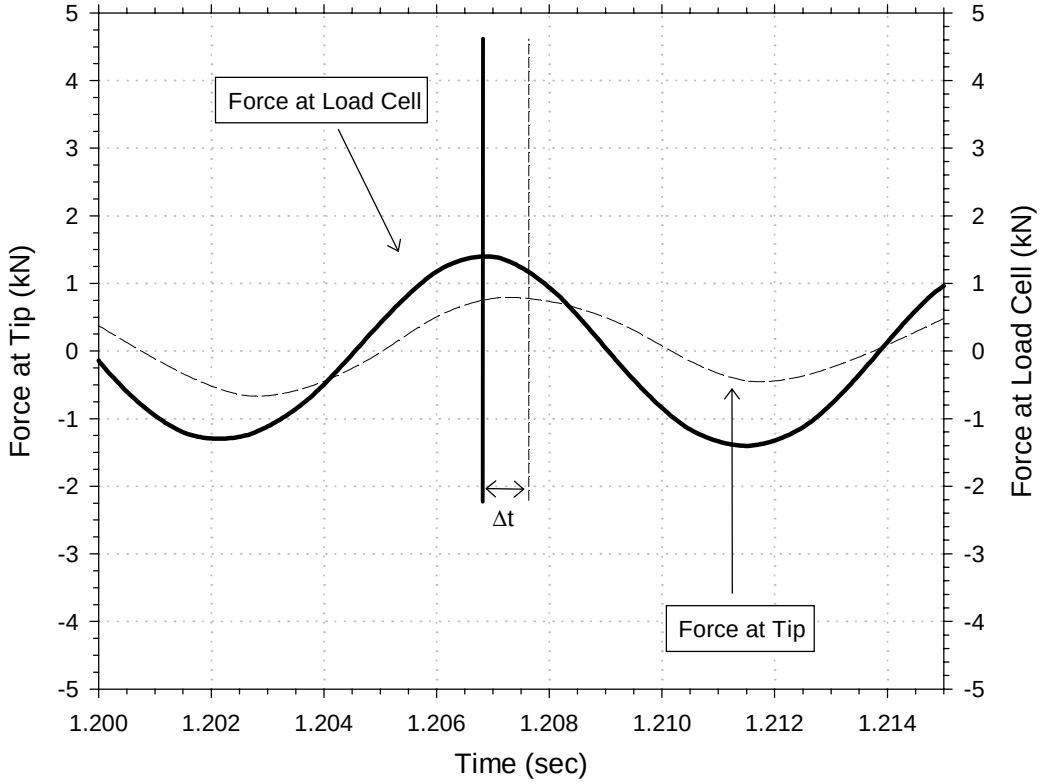

Figure 3.38 Comparison of Force Measured Through Load Cell to that Estimated at Tip Using Rotary Turbine Vibrator

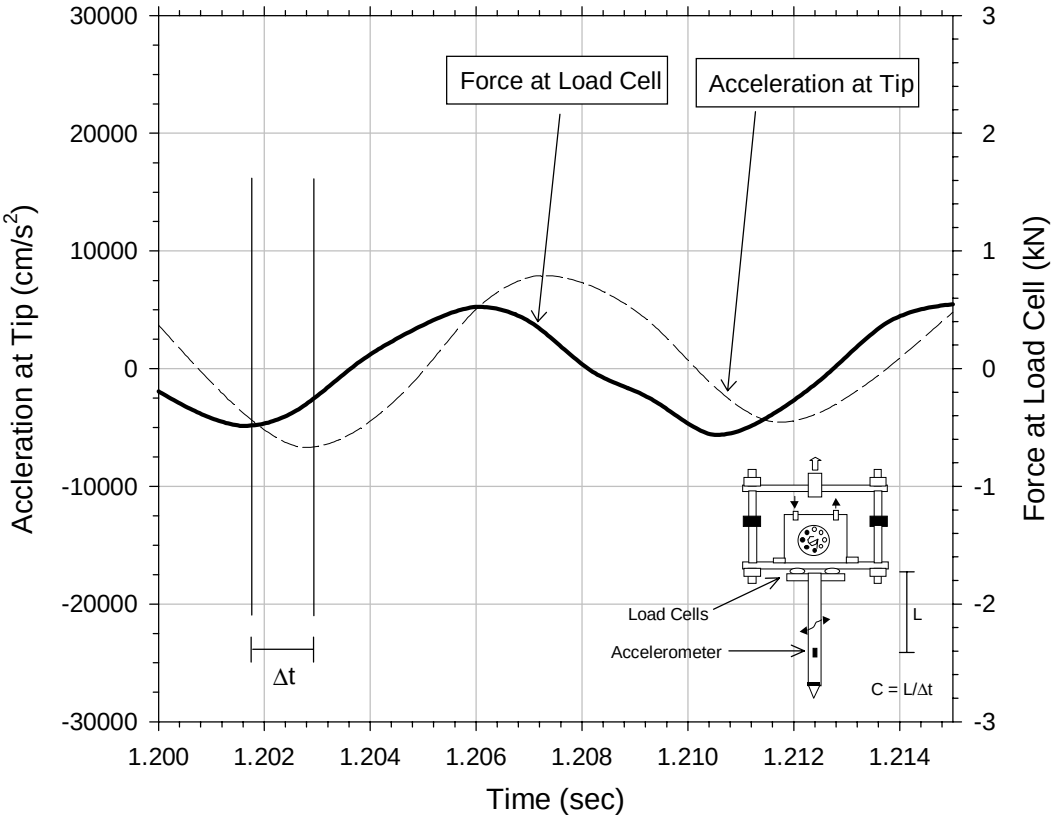

Figure 3.39 Proposed Approach for Estimating Wave Velocity

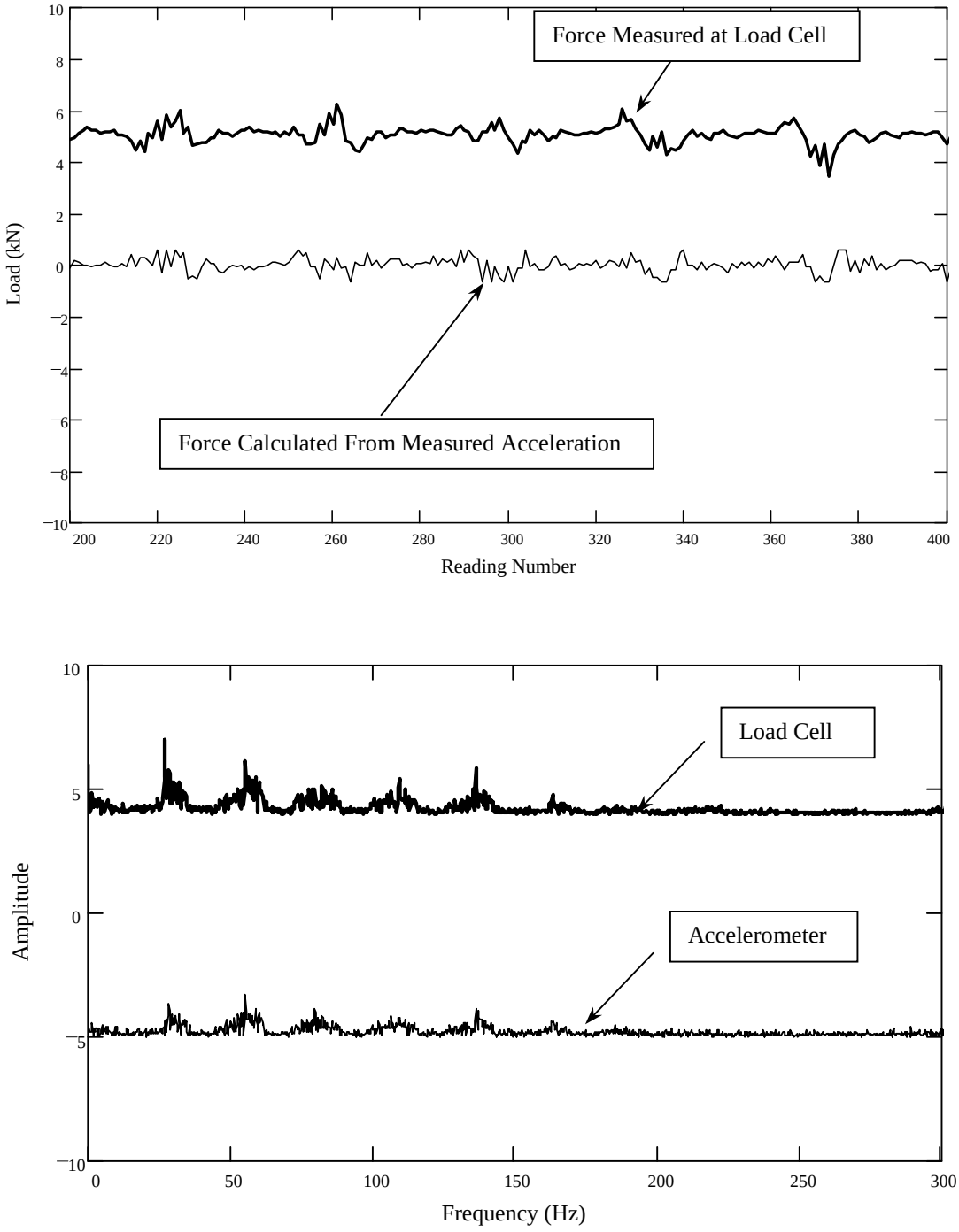

Figure 3.40 Representative Motion Generated by Counter Rotating Mass Vibrator

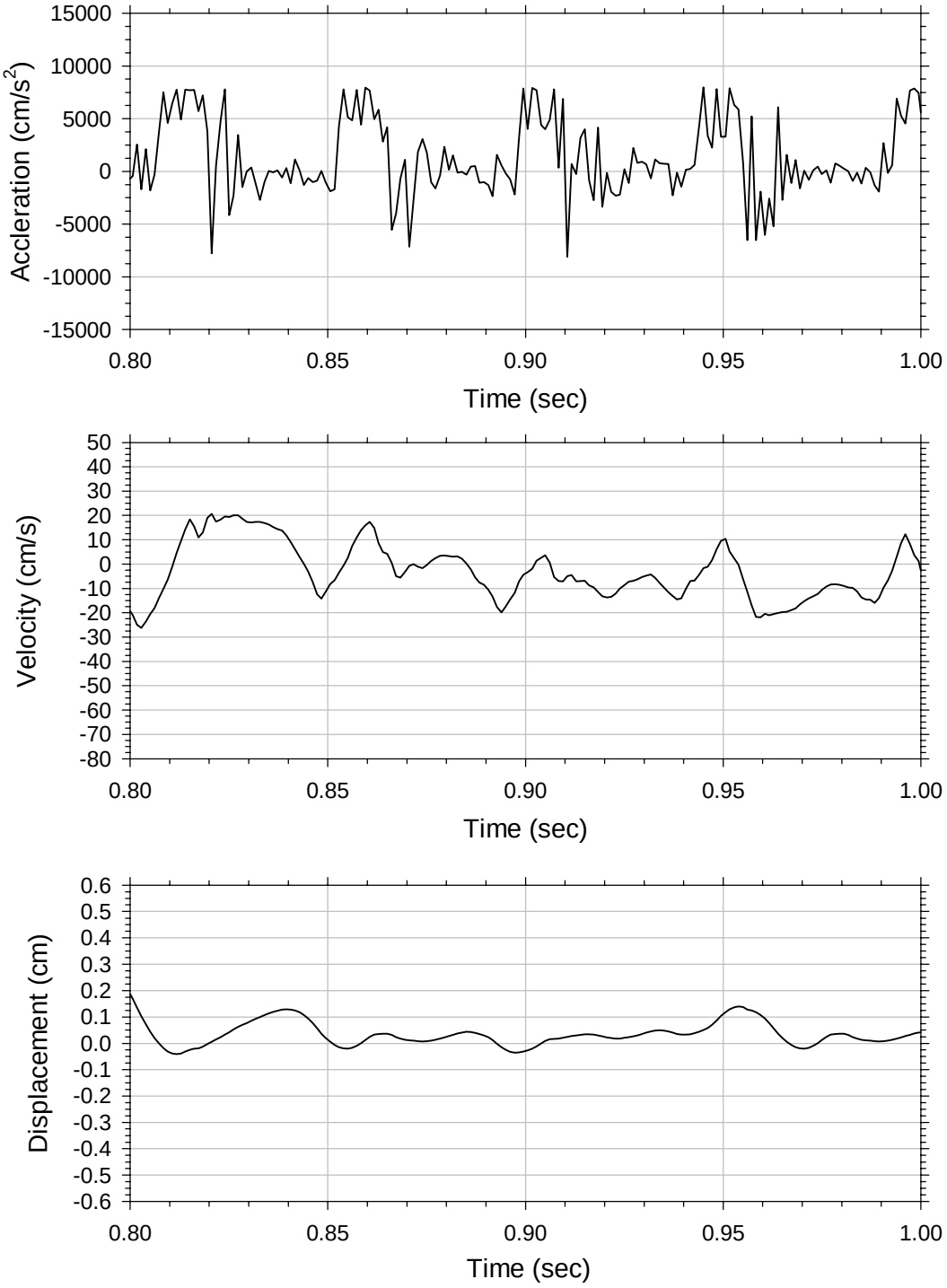

Figure 3.41 Representative Acceleration, Velocity, and Displacement Measured During Penetration at the Accelerometer Location Using Rotary Turbine Vibrator

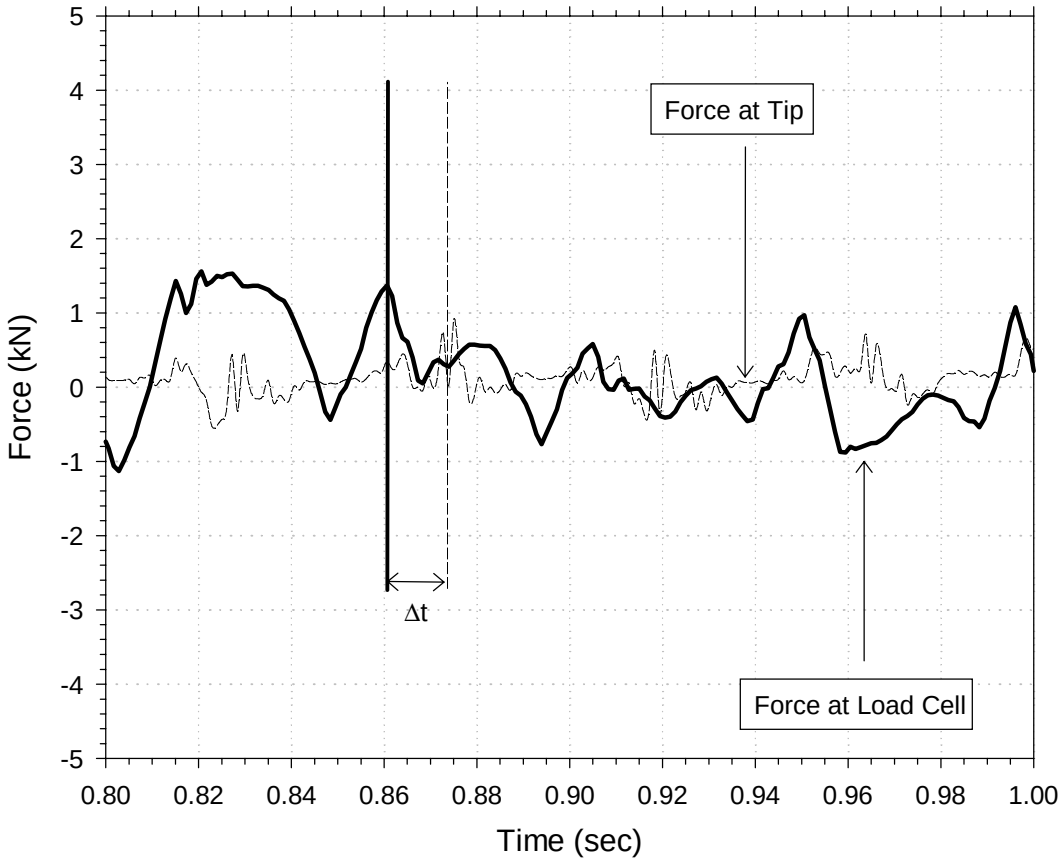

Figure 3.42 Comparison of Force Measured Through Load Cell to that Estimated at Tip Using Rotating Mass Vibrator